The geometry of active shortening in the northwest Himalayas and the implications for seismic hazard

Aisling O'Kane [1], Alex Copley [1], Supriyo Mitra[2] and Sam Wimpenny [1]

[1]*COMET, Bullard Laboratories, Department of Earth Sciences, University of Cambridge, Cambridge, CB2 3EQ, UK. E-mail: amo49@cam.ac.uk*
[2]*Department of Earth Sciences, Indian Institute of Science Education and Research Kolkata, Mohanpur - 74126, West Bengal, India*

SUMMARY

Large thrust faults accommodate the convergence between India and Tibet along the southern margin of the Himalaya and have a history of producing great earthquakes that cause widespread damage. Along most parts of the Himalaya, there is geomorphological evidence that these thrusts can rupture to the surface in $M_w > 8$ earthquakes. However, in the Himalayan state of Jammu & Kashmir (NW India), the thrust faults are blind and large-scale folding is the only expression of active deformation at the surface, making it difficult to assess the seismic hazard in this region. In this paper, we use field, satellite, and seismological observations to determine the fault geometry in Jammu & Kashmir. We then estimate the ground motions from potential earthquakes in the region using models of the seismic wavefield that would be generated if the thrust fault beneath Jammu & Kashmir were to rupture. We find that earthquakes that rupture the buried, shallow part of the locked Main Himalayan Thrust could generate peak ground velocities that are >3 times larger than earthquakes of the same magnitude on its deeper portions. We also model the ground motions that would result from the thrust fault geometries representative of different parts of the Himalayan arc. These simulations show that even seemingly minor variations in the shallow fault geometry can lead to large differences in the expected ground motions, highlighting the importance of accurately determining the shallow geometry of thrust faults along the margins of mountain ranges for estimating seismic hazard.

Key words: Geomorphology; Computational seismology; Earthquake ground motions; Earthquake hazards; Seismicity and tectonics; Folds and folding.

1 INTRODUCTION

Rapid urbanization in the Himalayan foothills and Indo-Gangetic Plains over recent decades has led to population pressures in growing cities (Tiwari *et al.* 2018), resulting in a vastly increased exposure and vulnerability of people and buildings to the ground shaking from earthquakes in the region (Fig. 1). These towns and cities are built on thick accumulations of foreland basin sediments, which are known to amplify earthquake ground motions (Bard & Bouchon 1985; Pandey & Molnar 1988; Rial *et al.* 1992; Joyner 2000; Meza-Fajardo *et al.* 2016; Bowden & Tsai 2017; Rajaure *et al.* 2017). Towns and cities that are located at the deformation front between the foreland basin and fold-thrust belt are particularly at risk from earthquakes that rupture the interface between the underthrusting Indian shield and the overlying Himalayan units at depth (known as the Main Himalayan Thrust; MHT), and the foremost splay fault in the megathrust system which connects to the MHT and outcrops at the surface (known as the Main Frontal Thrust; MFT).

Paleoseismic studies have found evidence for great (>M_w 8) surface-rupturing earthquakes in the 11th to 17th centuries along the MHT (Lavé *et al.* 2005; Kumar *et al.* 2006, 2010; Hossler *et al.* 2016; Wesnousky *et al.* 2017a, b; Pandey *et al.* 2021). Since the establishment of the instrumental record in 1900, five large earthquakes on the southern margin of the Himalaya have been recorded [(1) 1905 M_w 7.8 Kangra, (2) 1934 M_w 8.4 Bihar–Nepal, (3) 1950 M_w 8.6 Assam, (4) 2005 M_w 7.6 Kashmir and (5) 2015 M_w 7.8 Gorkha]. Some of these large earthquakes occurred on blind faults that did not rupture to the surface (Pandey & Molnar 1988; Ambraseys & Bilham 2000; Kumar *et al.* 2006; Kaneda *et al.* 2008; Avouac *et al.* 2015; Wesnousky *et al.* 2018). However, geomorphological observations from Sapkota *et al.* (2013), Bollinger *et al.* (2014) and Priyanka *et al.* (2017) suggest that the largest of these earthquakes, the 1934 Bihar–Nepal and 1950 Assam events, did rupture to the surface. These observations have led to the suggestion that ruptures on the MHT may have bi-modal behaviour, with the M_w 7 events breaking only the deeper sections of the fault and
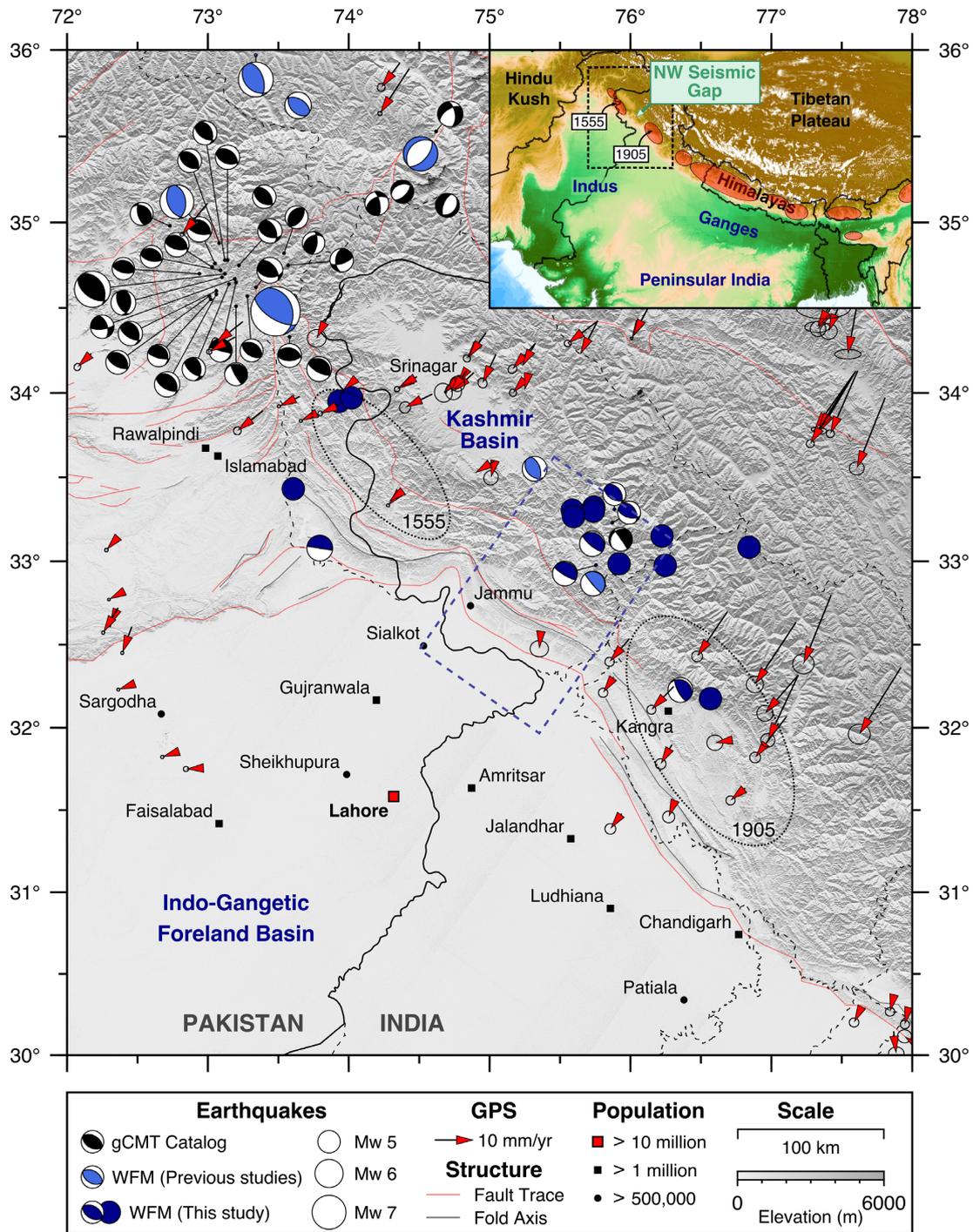
Figure 1. Map of the NW Himalayas illustrating the crustal seismicity and GPS velocity field in the region. Earthquake mechanisms were taken from the global CMT catalogue (Dziewonski *et al.* 1981; Ekström *et al.* 2012), this study and previous waveform-modelling (WFM) studies (Chen & Molnar 1983; Baranowski *et al.* 1984; Molnar & Lyon-Caen 1989; Sloan *et al.* 2011). Navy focal mechanisms illustrate the earthquakes where we could invert for a focal mechanism, whilst the navy circles represent earthquakes where we only determined the hypocentral depth and placed some constraints on the geometry of the nodal planes. Earthquake epicentral locations were taken from the ISC-EHB bulletin (Engdahl *et al.* 1998). Large-scale fault and fold axial traces were traced after Gavillot *et al.* (2016), Taylor & Yin (2009) and Styron *et al.* (2010), in addition to our field and satellite observations. GPS data was taken from Kundu *et al.* (2014) and Kreemer *et al.* (2014) and are shown relative to stable India. The line of control between Pakistan and India is marked in a solid black line, whilst state boundaries are illustrated in black dashed lines. The dashed navy box outlines the location of our computational model, and the two dashed black ellipses denote the 1555 and 1905 earthquake ruptures which bound the apparent NW Himalayan seismic gap and Surin Mastgarh Anticline. The inset map outlines the region of the main figure and the locations of historic earthquake ruptures (red ellipses) along the Himalayan arc after Bilham (2019).

the largest M_w 8 events rupturing the entirety of the fault to the surface (e.g. Dal Zilio *et al.* 2021).

The along-strike extent of the large historical and instrumentally recorded earthquakes have revealed that certain segments of the MHT have not ruptured in over 500 years, forming several apparent 'seismic gaps' along the Himalayan arc (see Fig. 1, inset). The state of Jammu and Kashmir (J&K) in the northwestern Himalaya sits within one of these seismic gaps, between the rupture areas of the M_w 7.6–8.0 1555 Kashmir and M_w 7.8 1905 Kangra earthquakes (Ambraseys & Bilham 2000; Ambraseys & Jackson 2003; Bilham 2019, Fig. 1, inset). At the surface, shortening along the range front in this area is expressed as kilometre-scale folding, as opposed to the surface-rupturing faults seen further east along most of the Himalayan arc (Gavillot *et al.* 2016; Thakur *et al.* 2019). The shallow fault geometry beneath these folds is therefore relatively poorly understood. Nonetheless, it is important to constrain the fault geometry, and how it relates to the shallow folding, in order to estimate the seismic hazard in the NW Himalaya. The depth of fault slip during large thrust earthquakes is one of the key factors in controlling the ground motions in foreland basin settings (O'Kane & Copley 2021).

In this study, we use seismological, structural, and geomorphological observations to constrain the geometry of the range front thrust system in the NW Himalayas of J&K. We focus on determining the dip and updip termination depth of the thrust faults beneath the Jammu section of the Himalayan foothills. We then use these results to construct models of seismic-wave propagation from earthquakes on these thrusts, and obtain estimates of the ground motions from potential earthquakes within the NW Himalaya seismic gap. We also conduct simulations using the fault geometry representative of other Himalayan regions to investigate how the evolution of deformation through space and time may influence the seismic hazard posed to any particular region along the margin of a mountain belt. We will first describe seismological results that constrain the geometry of the deeper portions of the thrust faults, then geological and geomorphological observations that constrain the shallow geometry. We then use these results to model the ground motions resulting from earthquakes on the possible fault geometries.

2 SEISMICITY IN THE NORTHWEST HIMALAYAS

The focal mechanisms and depths of earthquakes can be used to estimate the geometry of faulting at depth. We performed body-waveform modelling of eighteen $>M_w$ 5 earthquakes in J&K, which had data available from the Incorporated Research Institutions for Seismology (IRIS) and were of sufficient magnitude for clear signals to be recorded on broadband seismometers at teleseismic distances (see Table 1 for a list of events). Waveform modelling allows us to determine the strike, dip, rake, centroid or hypocentral depth, moment release and source-time function of each earthquake to a greater degree of accuracy than is possible from automatically-generated catalogues (e.g. Wimpenny & Watson 2020). Some of the events we have modelled have been studied previously using similar techniques, but we re-inverted the waveforms in light of new information regarding the velocity structure in the region (Bhattacharya 1992; Suresh *et al.* 2008; Mitra *et al.* 2011; Mahesh *et al.* 2013; Agrawal *et al.* in review; Bera *et al.* in review). For earthquakes where it was not possible to invert for a focal mechanism due to a lack of high signal-to-noise waveforms with good azimuthal coverage, we determined the earthquake depth only, but used the polarity

of the direct *P*-wave arrivals to place constraints on the geometry of the nodal planes. Our analysis of the moderate-magnitude seismicity in J&K complements the study by Paul *et al.* (2018) on the microseismicity in the region, and previous modelling of moderate-magnitude earthquakes (Baranowski *et al.* 1984; Molnar & Lyon-Caen 1989; Priestley *et al.* 2008; Mitra *et al.* 2014; Powali *et al.* 2020).

2.1 Methodology

2.1.1 Long-period body-waveform modelling

Two earthquakes in the region (the 2019 M_w 5.7 Mirpur and 2013 M_w 5.6 Kandosu earthquakes; earthquake numbers 03 and 07 on Fig. 2) had sufficiently clear teleseismic waveforms for us to invert for their focal mechanism, centroid depth and source–time function simultaneously using *P* and *SH* long-period waveforms. The methodology we used has been applied previously by Mitra *et al.* (2014) and Powali *et al.* (2020) to study earthquakes in J&K. Although we summarise the approach below, McCaffrey & Abers (1988) and Molnar & Lyon-Caen (1989) provide a more detailed account of the methodology.

We manually picked the *P*- and *SH*-wave arrival times on up to 50 broad-band vertical- and transverse-component seismograms from stations between 30 and 90 epicentral degrees, and filtered the waveforms to reproduce the response of a long period World-Wide Standardised Seismograph Network instrument (15–100 s). We then used the program MT5 (Zwick *et al.* 1994) to invert the long-period *P* and *SH* waveforms for the best-fitting point-source mechanism, the centroid depth and the source–time function. For each inversion, we used a starting model based on the global Centroid Moment Tensor (gCMT) catalogue solution (Dziewonski *et al.* 1981; Ekström *et al.* 2012) and constrained the moment tensor to be pure double-couple. Although the moment tensor is not particularly sensitive to the local velocity structure, the centroid depth estimates are. We used a 1-D seismic velocity model in the shallow crust of $V_p = 5.9$ km s^{-1} and $V_s = 3.4$ km s^{-1}, based upon 1-D velocity profiles derived from receiver function and surface wave dispersion studies across the NW Himalayas (Ni *et al.* 1991; Bhattacharya 1992; Mitra *et al.* 2006; Suresh *et al.* 2008; Mitra *et al.* 2011). An example of the minimum-misfit solution for the 24th September 2019 Mirpur earthquake is shown in Fig. 3.

For each earthquake, we performed a sensitivity analysis by fixing each earthquake parameter in turn, and re-inverting for the minimum-misfit solution whilst letting the other parameters vary (see Fig. S3b). Using this approach, we were able to identify the range over which each parameter produced an acceptable fit to the waveforms. We identified a number of trade-offs among the earthquake parameters, with the most important for this study being between the centroid depth and source–time function length (Christensen & Ruff 1985). We were able to constrain the centroid depths to within ± 3 km and the earthquake dips to $\pm 10°$ for the velocity model used, in line with previous studies using this method (e.g. Taymaz *et al.* 1990).

2.1.2 Broad-band and short-period depth-phase modelling

Where there were insufficient stations with clear long-period body-wave signals to undertake the modelling described above, we adopted a different approach and used the polarity of the direct *P*-wave arrival, and the delay time between the direct *P* arrival and

Table 1. Earthquake source parameters for events studied using waveform modelling. Epicentral locations are sourced from the ISC-EHB (Engdahl *et al.* 1998) bulletin. Earthquake magnitude is sourced from the gCMT catalogue where available (Dziewonski *et al.* 1981; Ekström *et al.* 2012), and otherwise taken from the ISC-EHB bulletin. For events that did not have an available gCMT focal mechanism, a representative mechanism was used in the modelling, chosen by closely following the fault plane solutions of neighbouring earthquakes after Molnar & Lyon-Caen (1989), Mitra *et al.* (2014) and Paul *et al.* (2018) who previously waveform modelled a select number of the earthquakes in the region (earthquakes denoted with an asterisk below). The waveform method used for each earthquake is outlined in column 11 with a corresponding supplementary figure reference followed in brackets. 'LP' denotes the earthquakes that were studied using long-period waveform modelling, 'BHZ' identifies those modelled using broadband seismograms, and 'SHZ' is assigned to earthquakes where modelling of short-period data from small-aperture seismic arrays was conducted. Errors denoted for earthquake depth and dip are independent of the errors associated with the velocity model. See the supporting information for a detailed discussion of each earthquake.

Ref	Date (YYYY–MM–DD)	Time (HH:MM:SS GMT)	Lon (°)	Lat (°)	Depth (km)	Strike (°)	Dip (°)	Rake (°)	M_w	Method
							Waveform modelling			
01	2021-01-11	14:02:03	75.59	33.30	6^{+1}_{-1}	-	45^{+0}_{-5}	-	5.1	BHZ(S01)
02	2020-02-26	15:04:08	76.25	32.98	15^{+2}_{-1}	-	40^{+5}_{-0}	-	5.0	BHZ(S02a), SHZ(S02b)
03	2019-09-24	11:01:54	73.79	33.08	10^{+3}_{-3}	275	01^{+9}_{-1}	086	5.7	LP(S03a,S03b), BHZ(S03c)
04	2014-06-13	13:32:51	75.60	33.27	11.5^{+4}_{-1}	-	30^{+15}_{-0}	-	5.2	BHZ(S04a), SHZ(S04b)
05*	2013-08-02	21:37:43	75.89	33.31	14^{+1}_{-1}	326	42^{+3}_{-12}	110	5.1	BHZ(S05a), SHZ(S05b)
06*	2013-08-02	02:32:48	75.87	33.23	15^{+2}_{-1}	327	42^{+3}_{-12}	122	5.1	BHZ(S06a), SHZ(S06b)
07*	2013-05-01	06:57:15	75.73	33.10	15^{+3}_{-3}	299	14^{+10}_{-6}	080	5.6	LP(S07a,S07b), BHZ(S07c), SHZ(S07d)
08	2011-08-23	01:22:57	76.84	33.08	13^{+1}_{-1}	-	35^{+10}_{-0}	-	5.3	BHZ(S08)
09	2006-05-26	00:41:39	76.22	33.15	9^{+1}_{-1}	-	40^{+5}_{-10}	-	5.2	BHZ(S09)
10	2005-10-15	04:32:19	73.96	34.02	14^{+1}_{-1}	-	15^{+0}_{-5}	-	5.2	BHZ(S10a), SHZ(S10b)
11	2005-10-15	04:24:04	73.95	34.03	13^{+1}_{-1}	-	15^{+0}_{-5}	-	5.3	BHZ(S11)
12	1993-09-15	15:08:14	75.74	33.32	8^{+1}_{-1}	-	30^{+15}_{-10}	-	5.0	BHZ(S12)
13	1990-12-25	03:56:46	75.74	33.30	3^{+1}_{-1}	-	45^{+0}_{-35}	-	5.5	BHZ(S13)
14*	1986-04-26	07:35:16	76.35	32.23	13^{+1}_{-1}	299	20^{+5}_{-5}	058	5.5	BHZ(S14)
15*	1980-08-23	21:36:49	75.76	32.98	16^{+1}_{-1}	293	10^{+5}_{-5}	082	5.5	BHZ(S15)
16	1980-05-01	05:43:10	75.92	32.99	13^{+1}_{-1}	-	30^{+10}_{-10}	-	5.2	BHZ(S16)
17	1978-06-14	16:12:04	76.57	32.18	32^{+1}_{-1}	-	25^{+5}_{-10}	-	5.3	BHZ(S17)
18	1978-05-07	10:32:25	73.61	33.43	14^{+1}_{-1}	-	01^{+9}_{-1}	-	5.3	BHZ(S18)

the depth phases *pP* and *sP*, to place constraints on the orientation of the nodal planes and determine the earthquake hypocentral depth. We used this method on all earthquakes in our study region that had suitably clear waveforms (see Table 1) and we were able to determine the hypocentral depths of $5.0 < M_w < 5.7$ earthquakes. This method has been widely used to determine the depths of earthquakes, and is described in detail elsewhere (e.g. Maggi *et al.* 2000; Emmerson *et al.* 2006; Sloan *et al.* 2011).

We used vertical-component broad-band seismograms for stations located at 30–80 epicentral degrees from the source, and picked the arrival time and polarity of the direct *P* wave. We fixed the earthquake strike, dip, and rake to the gCMT solution and generated synthetic seismograms for a subset of the stations with clear *P* and depth-phase arrivals using the program WKBJ3 (Chapman 1978; Chapman *et al.* 1988). The WKBJ3 program generates seismograms by ray tracing through a version of the global AK135 velocity model of Kennett *et al.* (1995), which we modified in the crust down to 40 km depth to be in line with regional 1-D velocity models (Ni *et al.* 1991; Bhattacharya 1992; Mitra *et al.* 2006, 2011; Suresh *et al.* 2008). In the modelling, we varied the attenuation propagation time $t*$ (Futterman 1962) between 0.5 and 1.0 s to fit the width of the observed signals. The observed and synthetic seismograms were aligned on the first peak after the direct *P*-wave arrival, and we varied the hypocentral depth until the synthetic seismograms visually matched the observed seismograms. An example of this type of analysis for the 1st May 2013 Kandosu earthquake in India is shown in Fig. 4. Typically, for a given velocity model, the hypocentral depths can be constrained to ±1–2 km using this method (Craig *et al.* 2012). In cases where the observed polarities of the first arrivals contradict those predicted by our assumed gCMT mechanisms, we adjusted the nodal plane dips (whilst keeping the strikes parallel to the local strike of the mountain belt, in accordance with the known mechanisms in the region)

to estimate what dip range is consistent with the available polarity observations.

For some moderate-magnitude earthquakes, the depth phases could not be clearly identified on individual seismograms due to the waveform amplitudes being similar to the background noise. For five events with M_w 5.0 to 5.2 and one M_w 5.6 earthquake, we improved the signal-to-noise ratio by stacking several short-period seismograms recorded at small-aperture seismic arrays (Craig *et al.* 2012). Within these arrays, the stations are close enough together that stacking can be performed using a simple linear time-shift based on the azimuth and horizontal slowness of the incoming plane-wave (e.g. Heyburn & Bowers 2008). We band-pass filtered the stacks between ∼0.1 and 5 Hz to extract the direct *P*-arrival and depth phases. The F-statistic assisted in the identification of the separate phases (Melton & Bailey 1957; Heyburn & Bowers 2008). We estimated the earthquake hypocentre depths by fitting synthetic seismograms to the filtered, stacked seismograms using the same method as described above. This method could typically constrain the earthquake depths to within ±1–3 km for a given velocity model. An example of this analysis for the 2nd August 2013 Kishtwar earthquake is shown in Fig. 5.

2.2 Patterns of seismicity in Jammu and Kashmir

The results of our seismological analyses, alongside the microseismicity located by Paul *et al.* (2018) and Agrawal *et al.* (in review), are shown in Fig. 2. We have used the ISC-EHB (Engdahl *et al.* 1998) determined epicentral locations for the earthquake events in this study, as these are generally accurate to within 10–20 km (Weston *et al.* 2018), which is a small uncertainty compared to the size of the Jammu region over which we analyse the seismicity distributions (∼150 km across-strike of the range front). The
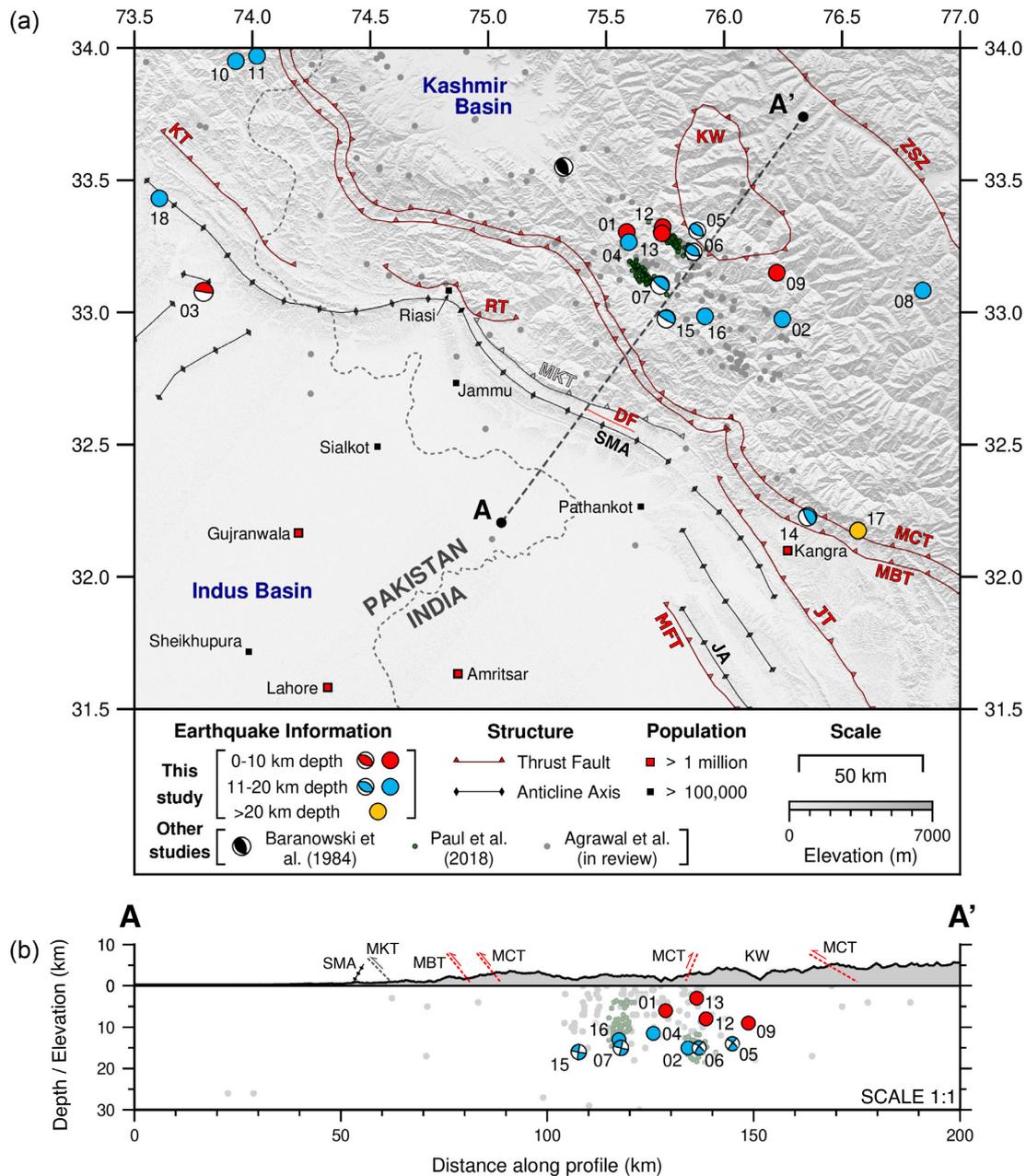
Figure 2. Seismicity across Jammu and Kashmir. (a) Moderate-magnitude earthquake focal mechanisms and distribution of microseismicity. Each moderate-magnitude earthquake has a label corresponding to the event number in Table 1. Published earthquake data is taken from Baranowski *et al.* (1984), Paul *et al.* (2018) and Agrawal *et al.* (in review). Major faults and folds are taken from Taylor & Yin (2009), Styron *et al.* (2010) and Gavillot *et al.* (2016), and a minor fault (DF) has been traced from our field and satellite observations. The labels are as follows: DF, Darung Fault; JA, Janauri Anticline; JT, Jawalamukhi Thrust; KT, Kotli Thrust; KW, Kishtwar Window; MBT, Main Boundary Thrust; MCT, Main Central Thrust; MFT, Main Frontal Thrust; MKT, Mandili Kishanpur Thrust; RT, Riasi Thrust; SMA, Surin Mastgarh Anticline; ZSZ, Zanskar Shear Zone. (b) Cross-section illustrating the depth distribution of the seismicity across the region of Jammu and Kashmir (within 50 km of the transect). The coloured focal mechanisms and circles represent earthquakes that have been modelled in this study, whereas the small grey and green circles are microseismic events that have been previously modelled by Paul *et al.* (2018) and Agrawal *et al.* (in review), respectively.

supporting information provides a detailed discussion of the modelling results for each event. The moderate-magnitude seismicity and microseismicity is mostly clustered in a region ~50–100 km NE of the range front, between the Kishtwar Window (KW) and the Main Central Thrust (MCT) (see Fig. 2). The largest earthquakes in this area have thrust- and reverse-faulting mechanisms with NW–SE trending nodal planes that strike parallel to the range front. The seismicity ranges in depth between 3 and 16 km, though

one event SE of Jammu has a hypocentral depth of 32 km (event 17 on Fig. 2). Southwest of the cluster of seismicity, near Jammu, there has been little recorded microseismicity beneath the range front and no moderate-magnitude earthquakes. However, further southwest of Fig. 2, in the foreland, the 1996 M_w 5.5 Nilore earthquake was recorded, with a centroid depth of 38 km (Maggi *et al.* 2000).

There is a distinct change in the nodal plane dips of the focal mechanisms as a function of distance from the range front. It is
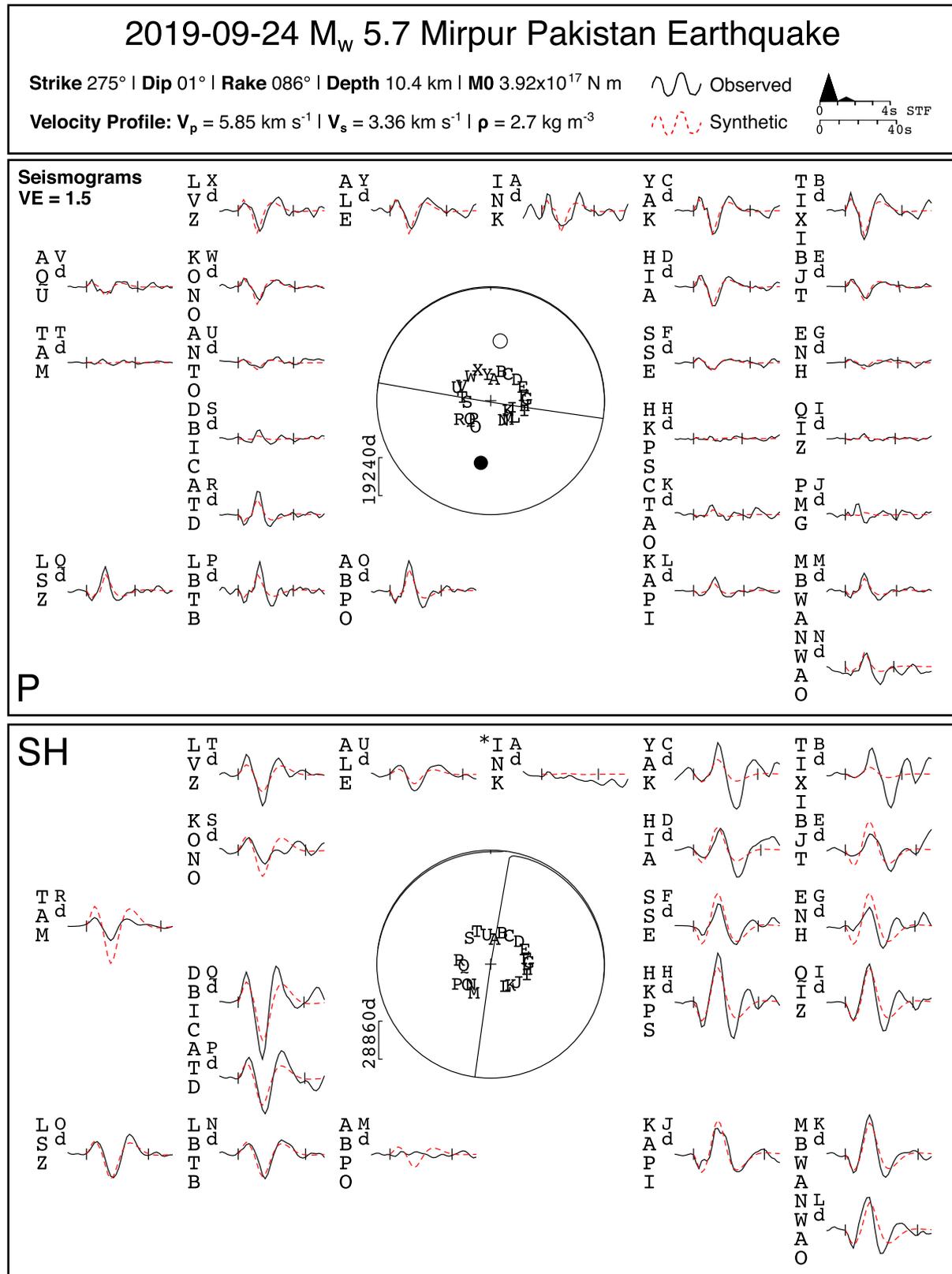
Figure 3. Minimum-misfit solution for the 24th September 2019 Mirpur Pakistan earthquake following the method outlined in Section 2.1.1. The earthquake parameters and velocity profile are presented in the top panel along with the source–time function (STF). A lower hemisphere projection of the *P* and *SH* nodal planes are illustrated in the middle and lower panels, respectively. Each panel also shows the observed and modelled seismograms for each station used in the inversion, and their 3–4 letter station code (positioned to the left of each seismogram). The *SH* waves from the station 'INK' (denoted with an asterisk) have almost zero amplitude due to being nodal on the *SH* focal sphere, and therefore this station was not used in the inversion. The two black tick marks on each seismogram show the time window over which the inversions were performed. The *P*- and *T*-axes were projected onto the focal sphere as a black and white circle, respectively.
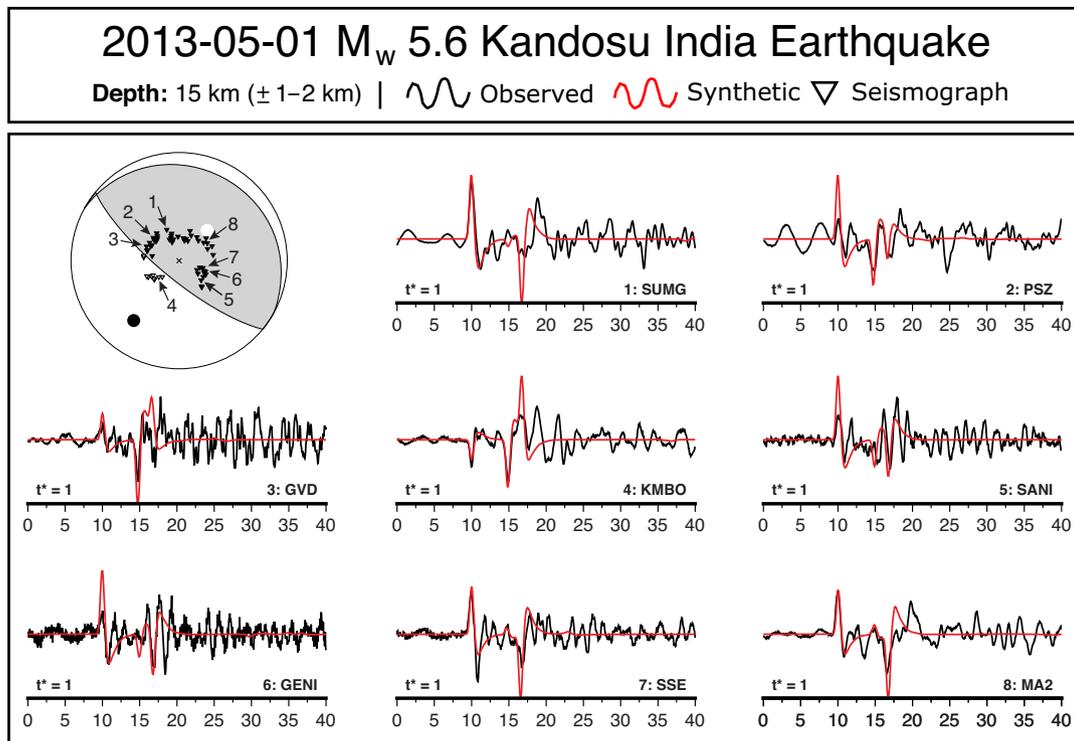
Figure 4. Depth-phase modelling of the vertical-component broad-band seismograms from the 1st May 2013 Kandosu India earthquake using the method outlined in Section 2.1.2. The hypocentral depth deduced for the earthquake is shown in the top panel. The *P*-wave focal mechanism is shown in the top left of the lower panel. Inverted triangles show the distribution of stations where we were able to identify clear *P*-wave arrivals. The solid triangles represent stations with compressional *P*-wave arrivals, and the light grey triangles signify stations with a dilatational *P*-wave arrival. The locations of the seismograms outlined in the bottom panel are labelled on the focal sphere. Each seismogram is shown with normalised amplitude and the *x*-axis represents time in seconds.

likely that the NE-dipping nodal planes represent the fault plane, as most of the structures at the surface have a SW vergence. Within the earthquake cluster NE of Jammu, the SW-most events (at distances of ∼100–120 km on Fig. 2b) have dips of ∼10–15° (e.g. events 7 and 15 in Fig. 2). Further to the NE, within the Kishtwar Window, the faults steepen, with dips in the range of 30–45° (at distances of 130–150 km on Fig. 2b). The change in fault dips in the Kishtwar Window region correlates with two NW–SE trending bands of shallow microseismicity identified by Paul *et al.* (2018). These bands have been suggested to reflect the internal deformation of the hanging wall as it moves over ramps in the MHT. Our waveform modelling results support this interpretation, as the dips of earthquakes vary systematically on either side of these bands of microseismicity. Some of the events we have studied have depths and mechanisms which suggest they occurred on steeper faults which lie in the hanging wall of the main Himalayan thrust fault. Taken together, the earthquake focal mechanisms imply that the MHT progressively steepens in dip towards the NE in the region between Jammu and the Kishtwar Window. Along-strike from J&K, an earthquake close to the range front in Pakistan has a subhorizontal dip (i.e. event 03 on Fig. 2), showing along-strike variability in the fault geometry.

The thrust earthquakes we have observed reach ∼110 km across-strike from the range front, to where the long-wavelength topography reaches ∼3500 m in elevation. The downdip limit of the seismicity, the ∼3500 m topographic contour, and the geodetically inferred locking line are observed to coincide with each other in other Himalayan regions along-strike to the SE (Ader *et al.* 2012; Bilham 2019). Such a pattern implies that the downdip limit of fault locking in the region NE of Jammu is similar to areas further

eastwards along the Himalayan arc. The earthquake slip vector azimuths align with the GPS velocities relative to India, showing that these faults can accommodate the shortening across J&K (Fig. 1).

Our seismological results only place constraints on the geometry of the deeper parts of the fault that have recently ruptured in earthquakes. In order to study the shallow geometry of the faulting, we make use of the geomorphology and geology of the region, which we describe later.

3 TECTONIC GEOMORPHOLOGY

Previous studies of the NW Himalayas in J&K have suggested that the shortening to the north of Jammu, where there is a prominent cusp in the range front topography near the town of Riasi (see Fig. 6), is partitioned roughly equally between the Riasi Thrust (RT) (6–11 mm yr^{-1}) and the Surin Mastgarh Anticline frontal fold (6–9 mm yr^{-1}, Vassallo *et al.* 2015; Gavillot *et al.* 2016, 2018; Mugnier *et al.* 2017). The distribution of shortening north of Jammu contrasts with the rest of the Himalayan arc east of Kangra (see Fig. 1), where the India–Asia convergence is accommodated primarily by the Himalayan Frontal Thrust (Lavé & Avouac 2000; Kundu *et al.* 2014; Gavillot *et al.* 2016; Jade *et al.* 2020; Ghavri & Jade 2021). We therefore studied the region between Jammu and Udampur (southeast along-strike of Riasi town, see Fig. 6), both in the field and using satellite-derived elevation models and imagery, to establish whether shortening in this region is distributed across multiple structures.

Southeast of Riasi, signs of Quaternary slip in the form of offset fan surfaces, river terraces, or the presence of fault scarps along the
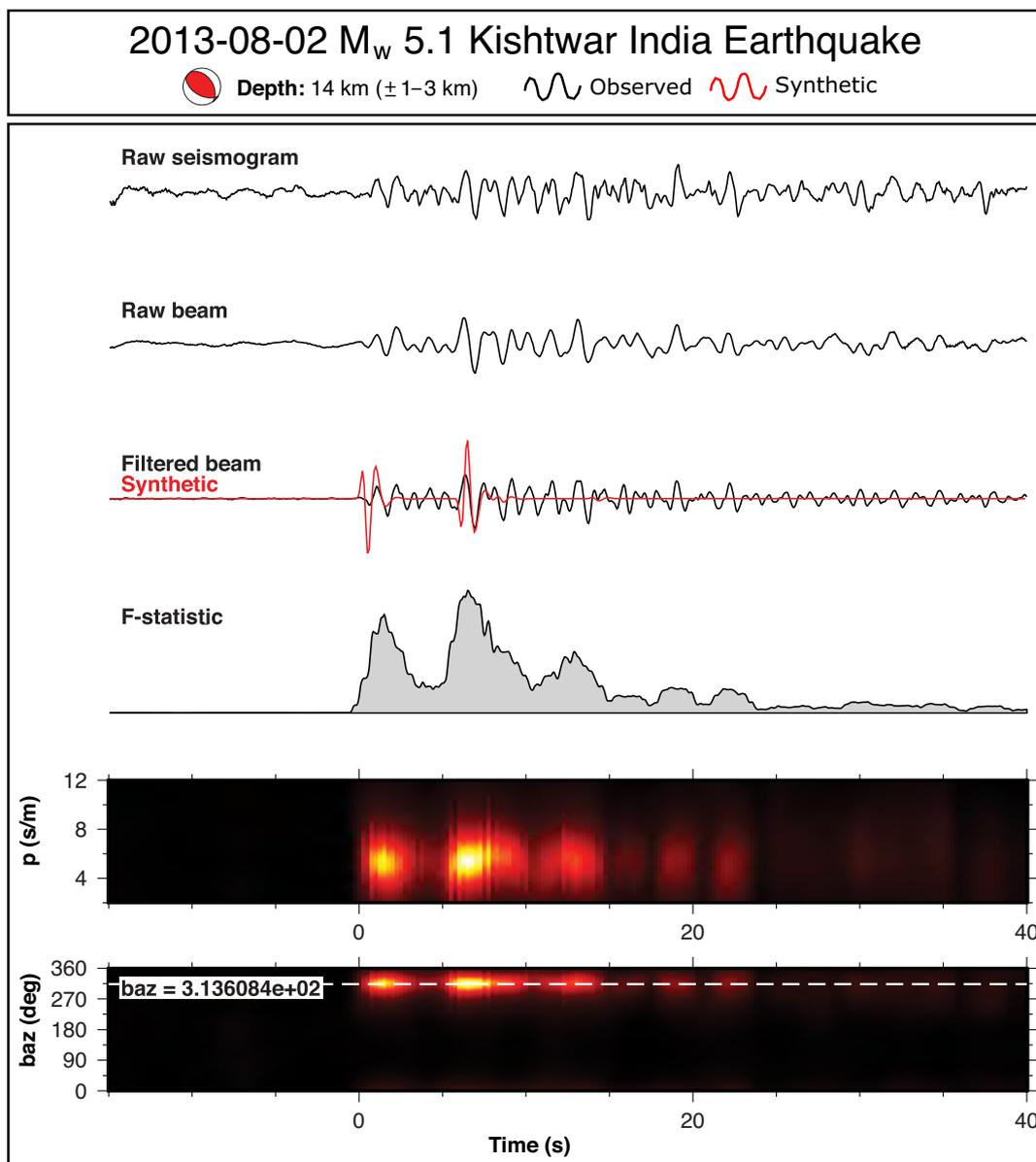
Figure 5. Depth-phase modelling of the vertical-component, short-period seismograms from the Alice Springs Array in Australia for the 2nd August 2013 Kishtwar India earthquake using the method outlined in Craig *et al.* (2012) and in Section 2.1.2. The focal mechanism and hypocentral depth used to generate the synthetic seismograms are shown in the top panel. The lower panel shows a raw vertical-component seismogram from the array, the stack (beam) of the array seismograms, and a band-pass filtered version of the stack. The F-statistic of Heyburn & Bowers (2008) is also shown, showing a clear signal ~6–7 s after the direct *P*-wave arrival. We also performed the stacking over various backazimuths (baz) and horizontal slownesses (*p*) to confirm that the energy after the direct *P*-wave arrival was coming from the same direction as the direct *P*-arrival (which is expected for the depth phases). We interpret the arrival ~5–6 s after the direct arrival to be the *pP* depth phase, which would be consistent with a depth of 14 ± 2 km and the gCMT focal mechanism.

mapped position of the Riasi Thrust (here known as the Mandili Kishanpur Thrust; MKT), are absent. In the field and on satellite-derived topographic datasets and imagery, geomorphic surfaces cross the fault with no signs of offset. The region which shows documented active shortening at Riasi is also the only part of this fault that has exhumed Precambrian limestones to the surface [e.g. see fig. 2 in Gavillot *et al.* (2018)]. It is therefore likely that to the SE of Riasi the shortening has been transferred to either the Surin Mastgarh Anticline (SMA) frontal fold (and underlying faulting) to the south, or onto faults within the Himalayan interior such as the Main Boundary Thrust or Main Central Thrust. We hypothesise that the shortening has been transferred south onto the SMA, due to the lack of documented active faulting within the range to the

north. Below we test this hypothesis by examining the structure and morphology of the SMA in the area SE of Jammu.

3.1 Field and satellite observations

The SMA is cut by a number of SW-draining rivers that preserve late Quaternary terraces along their margins. The morphology of these terraces can be used to test models for the style of shortening in the region (e.g. Lavé & Avouac 2000). We used a 12-m TanDEM-X global digital elevation model (DEM) to identify and map terraces along the Tawi, Ujh and Ravi rivers (Fig. 6). For each river, we
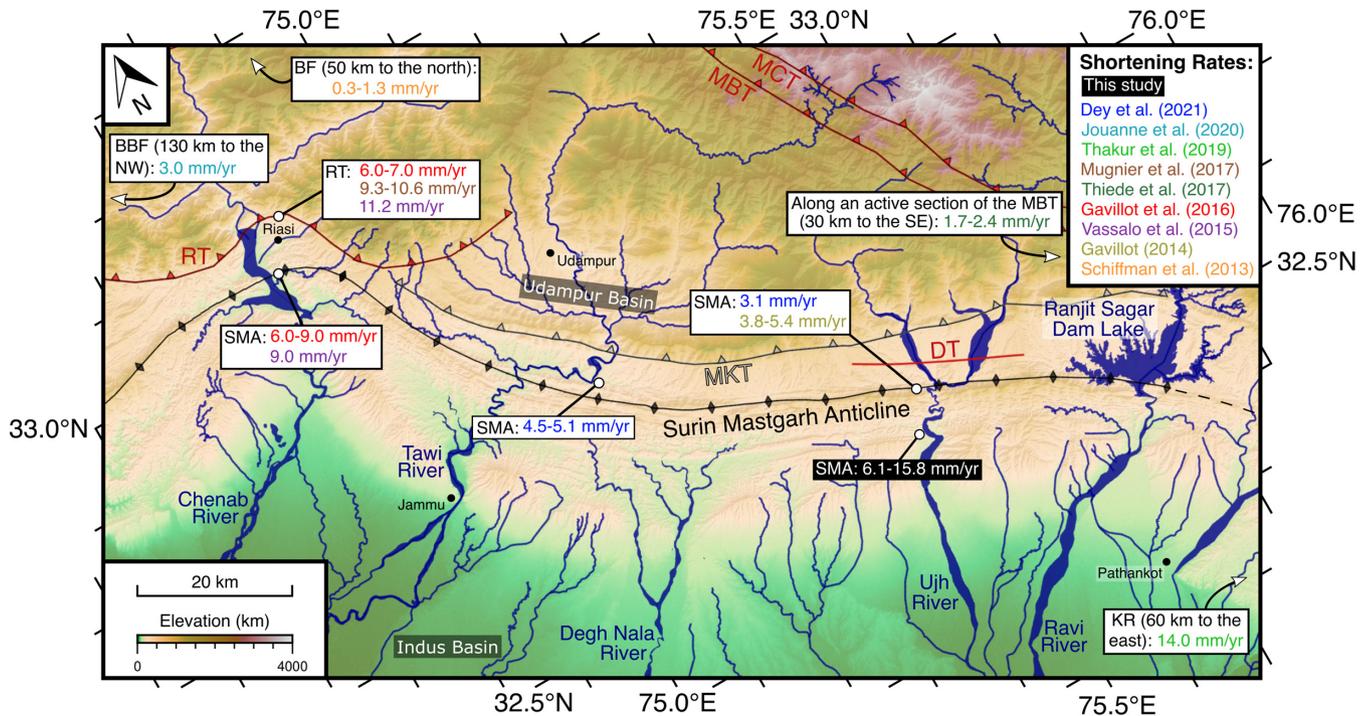
Figure 6. Topography and structure of the Surin Mastgarh Anticline (SMA), NW Himalaya. Major faults and the anticline fold axis were traced from Gavillot *et al.* (2016) and our field observations. Faults are labelled as in Fig. 2. Our estimated horizontal shortening rate on the fault underlying the SMA is annotated in the black text box. Published shortening rates attributed to other active structures in the Jammu and Kashmir region are noted in white text boxes with the structures annotated as follows: BF, Balapora Fault; BBF, Balakot-Bagh Fault; KR, Kangra Reentrant.

traced the edges of the individual terraces from the DEM and optical satellite imagery, and confirmed the terrace locations during fieldwork. By comparing the terrace heights above the present-day river bed as a function of distance perpendicular to the range front, we can reconstruct the deformation of these terraces since they were formed.

An example of the terraces along the margins of the Ujh river is shown in Fig. 7. The river profile shows a general concave-up shape, the main disturbance to which is the zone of entrenched meanders as the river passes through the core of the SMA. At the southern margin of the anticline, the terrace level increases in height above the river to ∼15–25 m over a horizontal distance of ∼2 km. Our field observations indicated that the terraces were cut into gently dipping Upper Siwalik conglomerates, which are themselves uplifted river deposits. We suggest that this short-wavelength change in terrace height records the outer zone of tectonic uplift, as there is no likely alluvial cause for such a sudden change in terrace elevation given the wide, low-gradient river valley where it drains into the plains of the foreland basin. The terrace height above the river (green lines on Fig. 7c) remains roughly constant to the north of the range front, with perhaps a slight increase in elevation, until the core of the anticline is reached, where no terraces are preserved in the highly erosive landscape. It is not possible to correlate the terraces across this region, but Fig. 7 shows that on the northern limb of the anticline there is a clear pattern of terrace height above the river increasing with distance along the profile. This observation implies increasing uplift rates to the northeast. Such a pattern contrasts with the commonly observed geometry of river terrace heights being at a maximum along the axis of a growing anticline and decreasing into the fold limbs (Molnar *et al.* 1994; Ainscoe *et al.* 2017). Equivalent analyses carried out for the Tawi and Ravi rivers are shown in Figs S19 and S20, respectively. These records are more fragmentary

due to the locations of the preserved terraces, but conform to the same pattern as seen along the Ujh river.

The constant terrace height above the river observed throughout the southern limb of the SMA implies that the uplift is not due to folding, in which case the uplift would vary across-strike, but instead due to faulting. A single, planar fault surface at depth would result in a spatially consistent pattern of uplift at the surface. In this situation, the short-wavelength decrease in terrace elevation at the southwestern end of the profiles would represent localised warping of the shallow sediments close to the fault tip. Furthermore, the increase in terrace heights above the river at the northeastern end of the profiles may imply a steepening dip of the fault in this region. Such an inference is supported by the presence of a minor fault that offsets the river terraces in this region. As shown in Fig. 8, a fault scarp that accommodates south-side-up motion offsets the terraces, although we were not able to establish the dip direction of the fault due to a lack of suitable exposure. Aravind *et al.* (2022) observed this fault during their field investigation and classified it as a bending-moment resultant normal fault. Dip-slip faulting within the hanging wall of the thrust directly beneath this location is consistent with the accommodation of an increase in dip on an underlying fault surface towards the northeast.

3.2 Implications for tectonic uplift rates and NW Himalayan structure

The terrace heights above the Ujh River can be used to deduce the tectonic uplift rate in the region. If we assume that, south of the core of the anticline, the river has maintained a consistent profile since the terraces were formed, then the amount of river incision can be presumed to approximate the tectonic uplift since the terrace abandonment. Although we could not locate appropriate material
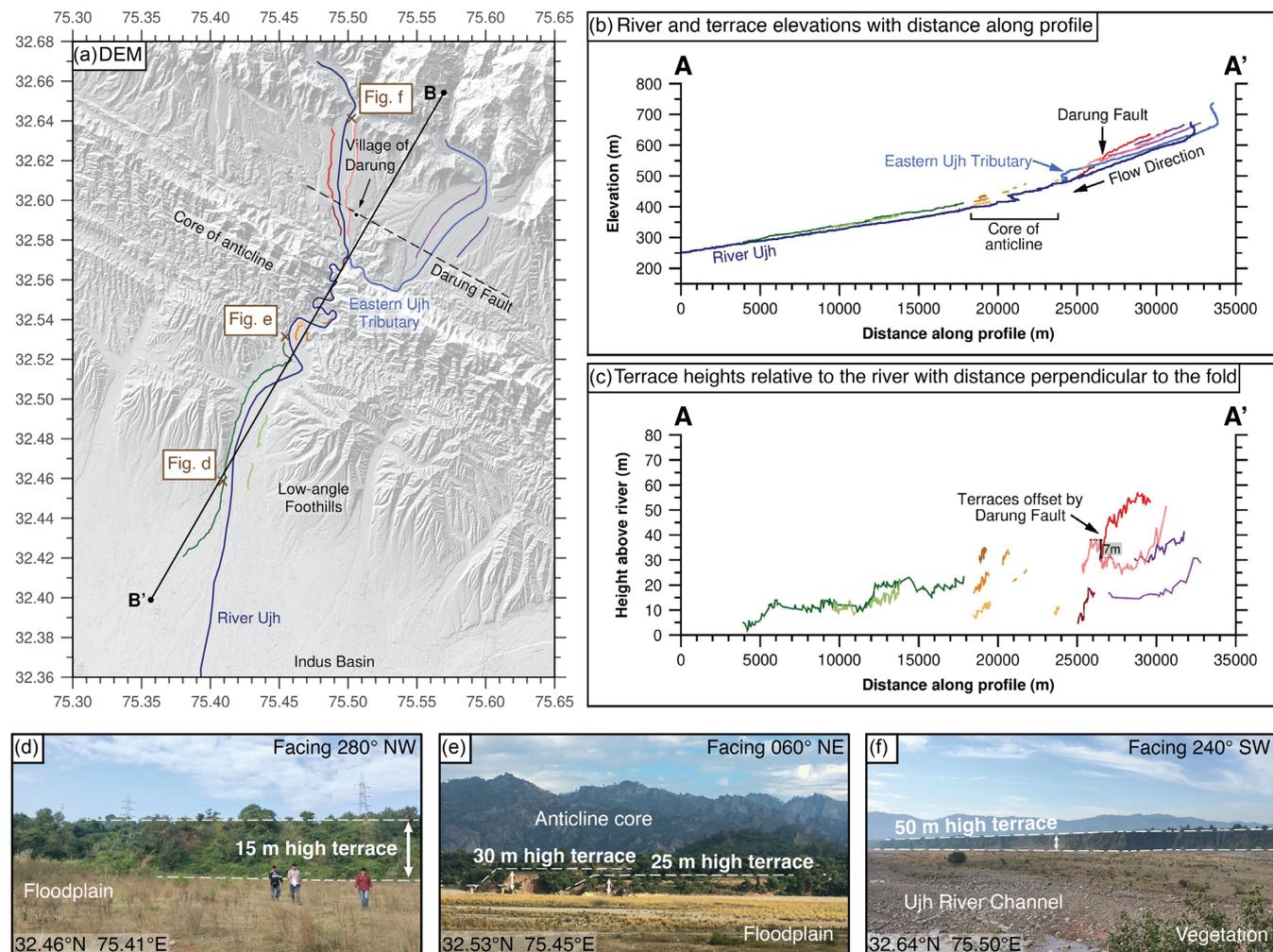
Figure 7. Geomorphological observations across the Surin Mastgarh Anticline. (a) DEM of the topography around the River Ujh approximately 60 km SE from Jammu (Fig. 6). The blue line represents the river's course and the coloured lines represent the edges of individual terraces. (b) Cross-section taken parallel to the shortening direction across the region, showing the river and terrace elevations with distance along the profile. (c) The terrace heights above the river with distance along the profile. Photographs in d, e and f show a selection of the terraces identified in the field.

during our fieldwork to date the terraces, it is likely that the terraces are Holocene–Pleistocene in age given that similar terraces on nearby river systems have ages of 10–20 kyr (Tawi River; Dey *et al.* 2021, Preprint) and 4–36 kyr (Chenab River; Vignon *et al.* 2017). Therefore, we assume a range of terrace ages between 4 and 36 kyr.

Using the lowermost, continuous terraces along the Tawi, Ujh and Ravi rivers as proxies for uplift, dividing the terrace heights above the rivers by a range of possible terrace ages yields an estimate for the uplift rate. The river Ujh terraces yielded vertical uplift rates in the range of 0.5–5.0 mm yr^{-1} across the southern limb of the SMA, based on an average terrace height of 20 m (Fig. 7c). Similarly, terraces along the Ravi river in the southern limb of the SMA indicate vertical uplift rates of 0.4–3.8 mm yr^{-1}, based on a terrace height of 15 m (see Fig.S20). Terraces along the Tawi river in the northern limb of the SMA indicate uplift rates of 0.3–2.5 mm yr^{-1} based on a 10 m high terrace (see Fig.S19). If it is assumed that the lowermost, laterally continuous terraces represent the 8–15 kyr end-glacial terrace, as is the case elsewhere in the Himalaya (Lavé & Avouac 2000; Richards *et al.* 2000; Mehta *et al.* 2014), then the corresponding estimated rates of uplift are 1.3–2.5, 1.0–1.9 and 0.6–1.3 mm yr^{-1} based on the Ujh, Ravi and Tawi

river terraces, respectively. These estimates are of the same order of magnitude as the Gavillot *et al.* (2018) estimated exhumation rate in the core of the SMA of ∼1 mm yr^{-1}, derived using low-temperature thermochronology.

The uplift rates can be used to estimate the horizontal shortening rate along the fault beneath the SMA. In the case where the terraces have been uplifted by faulting, the horizontal shortening rate v_s will be related to the dip of the fault θ and the terrace uplift rate v_u by: $v_s = v_u / \tan(\theta)$. The simplest possible fault geometry is of a constant-dip plane connecting the range front to the low-angle seismicity at depth, which in this case would be required to dip at 9–12°. If it is assumed that the prominent laterally continuous terrace level discussed above represents the 8–15 kyr end-glacial terrace, as is common throughout the NW Himalaya (Phillips *et al.* 2000; Owen *et al.* 2002), and consistent with the 10 kyr terrace age that Dey *et al.* (2021, Preprint) determined for the Ujh river, then the uplift rate in the location of the Ujh river is 1.3–2.5 mm yr^{-1}, and the estimated horizontal shortening rate is 6.1–15.8 mm yr^{-1}. However, the observations presented above imply a steepening of dip on the NE flank of the SMA, in which case the dip of the fault beneath the region of the terraces on the SW flank of the fold will be lower than this average value, and the rate of shortening will be
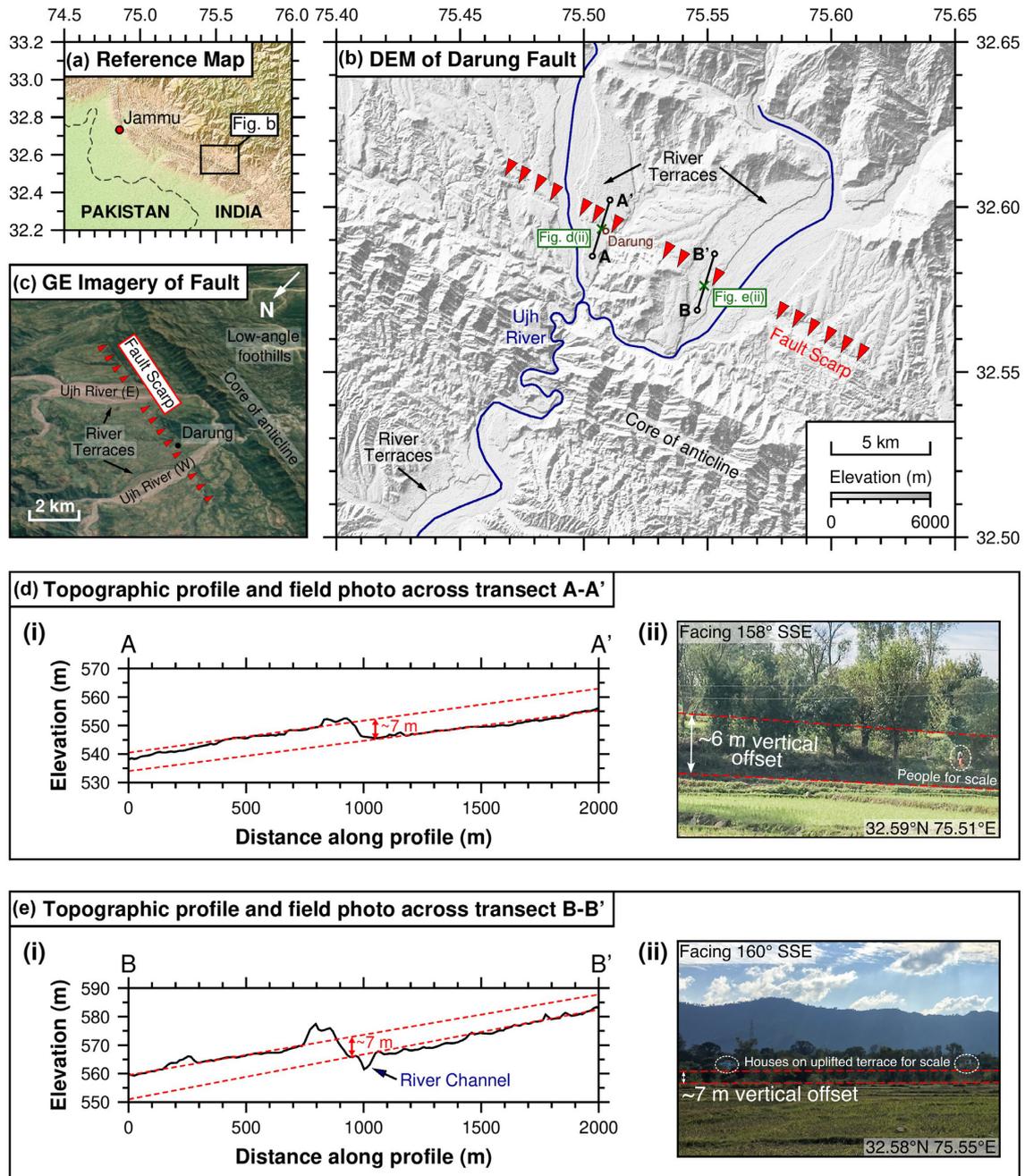
Figure 8. Active faulting on the northeastern margin of the Surin Mastgarh Anticline. (a) Inset map showing the location of the DEM in (b). (b) DEM of the Darung fault which offsets terraces along the western and eastern banks of the Ujh river. Red triangles mark the trace of the fault. (c) Google Earth satellite imagery of the fault. Panels (d) and (e) show topographic profiles and field photos for two locations where we identified offset terraces in the field.

towards the upper end of our range of estimates. A lower limit on the fault dip beneath the SMA can be approximated by not allowing the estimated rate of shortening to exceed the total convergence across this part of the Himalaya (12–14 mm yr^{-1}, Kundu *et al.* 2014). If the largest continuous terrace represents ages of 8–15 kyr, then the lower dip limit is 5–$10°$ for a convergence rate of 14 mm yr^{-1}. If the prominent terrace level is older, then this lower dip limit decreases (e.g. to $\sim3°$ for terrace ages of 25–30 kyr). Therefore, although we are not able to uniquely determine the shallow fault dip or the convergence rate in the region, the available information indicates that the majority, or all, of the convergence, is accommodated by the fault underlying the SMA, which dips at an angle of 3–$10°$ under

the SW limb of the SMA, and increases in dip to the NE. The more fragmentary terrace records on the Tawi and Ravi rivers preclude as detailed an analysis, but their similar elevations to the Ujh terraces imply similar shortening rates (although the underlying fault dip may change towards the ends of the fold).

The depth to the updip tip of this buried fault can be estimated from the terrace morphology by using the length scale over which the terrace heights decrease at the southern end of the profile in Fig. 7(c). The chosen geometrical model for the deformation plays a role in controlling the estimated termination depth. For example, for a 'tri-shear' model of the deformation beyond the fault tip (Erslev 1991; Hardy & Ford 1997; Allmendinger & Shaw 2000), if the

tri-shear angle is 30° as commonly suggested for a thrust fault, then the resulting estimate to the depth of the fault tip is ~2.5 km. Other models of fold production (e.g. fault-bend folds; Suppe 1983) would result in values that are different in detail, but for our purposes the 2–3 km length scale over which the terrace height above the river changes implies a depth to the updip fault tip of a similar value (i.e. 2–3 km).

3.3 Present-day thrust geometry in Jammu

The seismological and geomorphological results presented above suggest that present-day shortening in the Jammu region is accommodated by motion on a buried, low-angle thrust fault that underlies the SMA (Fig. 9). This fault has an updip termination near the edge of the range front at a depth of ~2.5 km, warping the terraces above it. The thrust dips northeastwards at 3–12°, as indicated by the terrace uplift rates coupled with the necessity to connect to the seismologically-estimated fault location to the NW. Northeast of the SMA core, the fault steepens in dip, as indicated by an increase in terrace heights above the rivers, and the presence of minor faulting on the NE flank of the SMA. The steeper dip then projects northeastwards to the cluster of earthquakes ~100 km NE of the range front (Fig. 9). Beneath the higher Himalaya, the thrust fault geometry may change further, but it is likely that the MHT is creeping and unable to rupture during great earthquakes in this area (Pandey *et al.* 1999; Stevens & Avouac 2015; Dal Zilio *et al.* 2021), and our methods, therefore, do not allow us to constrain the geometry.

4 GEOLOGICAL STRUCTURE OF THE SURIN MASTGARH ANTICLINE

The seismicity and the relatively spatially uniform uplift of the river terraces imply that the convergence in the Jammu region is currently mostly accommodated by motion on a single major fault at depth. However, the surface geology in the region is characterised by long-wavelength folding. In this section, we describe the structure of the folding and explore the relationship between folding and faulting along the range front.

The fold is expressed in Siwalik units, which we identified in the field using the lithological descriptions of Burbank *et al.* (1996), Powers *et al.* (1998) and Gavillot *et al.* (2016, 2018). The Lower Siwaliks are predominantly composed of red mudstones, the Middle Siwaliks of grey, massive, cross-bedded sandstones with some interbedded mudstone layers, and the Upper Siwaliks of conglomerates and sandstones. This sequence is interpreted to represent the evolution of sedimentary environments within the foreland basin during the encroachment of the Himalayan mountain belt (Burbank *et al.* 1996; Mugnier *et al.* 1999; DeCelles *et al.* 2001).

During fieldwork, we collected measurements of bedding strike and dip along three transects across the fold, and in a selection of intervening locations (Fig. 10). All strikes were parallel to the fold axis, as shown by the poles to bedding illustrated on the stereonet insets in Fig. 10. The bedding showed a distinctive pattern of increasing dip towards the axis of the fold, where there was an abrupt change in the younging direction in the near-isoclinal fold core. The dips then reduced on the far side of the fold, as also discussed by Aravind *et al.* (2022). Based upon the distribution of dips in the fold core, we suggest that the fold is likely to represent the lower portion of 'lift-off' folding produced by shortening above a weak decoupling layer, with the upper lobes having been removed by erosion (Mitra 2003; Hardy & Finch 2005, see Fig. 10d, inset). The Lower

Siwalik mudrocks exposed in the fold core were highly deformed in places, exhibiting striations and plentiful hydrothermal veining, and may well represent a decoupling layer beneath the more competent Middle and Upper Siwalik units. Such a geometry means that we are not able to estimate the total amount of shortening across the fold. However, we can estimate the depth to the base of the competent Middle Siwalik sandstones on the SW margin of the fold, by assuming constant bed thicknesses in the Middle and Upper Siwaliks and using the measured surface dips shown in Fig. 10. We estimate a depth to the base of the Middle Siwaliks at the southern margin of the fold of approximately 6 km, similar to a detachment depth of 8 km that Aravind *et al.* (2022) determined from a seismic reflection survey across the fold hinge north of Jammu. The assumption of constant bed thicknesses, although justified by the lack of visible internal strain observed in the field, limits the accuracy of this estimate. However, for the purposes of our discussion below, the key finding is robust, that the depth to the base of the Middle Siwaliks on the SW margin of the thrust is deeper than the ~2–3 km estimate for the updip termination of the currently active fault.

The above analysis raises two points about the geometry and evolution of deformation. First, the heights of the river terraces do not reflect the bedding dips. The river terrace uplift is roughly constant across the southern limb of the fold, in locations where the bedding dips are increasing from subhorizontal to subvertical. This comparison is in agreement with our inference above that the terrace uplift is caused by Holocene–Pleistocene faulting, rather than folding. Secondly, the estimated depth to the updip tip of the faulting calculated using the river terrace geometries (~2.5 km) is significantly less than the depth to the base of the competent Middle Siwalik units on the southern margin of the fold (~6 km). These analyses can be reconciled if the shortening in the region was previously dominated by folding, and the fold has since been cut through by faulting. This evolution of the deformation pattern has been observed in other mountain belts (Emami *et al.* 2010; Hansman & Ring 2018), and may represent either the evolution of material properties of the rocks involved, or the outwards propagation of low-angle faulting in order to limit the gravitational potential energy contrasts that develop as a result of convergence and thickening.

5 SEISMIC WAVE PROPAGATION MODELLING

In this section, we use seismic-wave-propagation modelling to estimate the earthquake-induced ground motions in the Jammu region that would result from rupture on the low-angle thrust fault beneath the SMA. We do not suggest that our results represent the ground motions that will definitely occur during the next major earthquake in the region, which depend upon a number of parameters of the earthquake that it is not possible to accurately know in advance (e.g. the amount of slip and the frequency content of the radiated waves, as discussed in more detail below). We instead model one plausible earthquake scenario, based on the logic presented below, and use this situation to investigate the role that fault geometry plays on the resulting ground motions.

Wave-propagation modelling has become an increasingly popular method of hazard assessment, because developments in computational power and numerical methods mean it is now possible to simulate the seismic wavefield at high frequencies, over large areas, with arbitrarily complex sources and material properties. Therefore, this type of modelling can take into account geological structures, such as earthquake source geometries and lithological heterogeneity
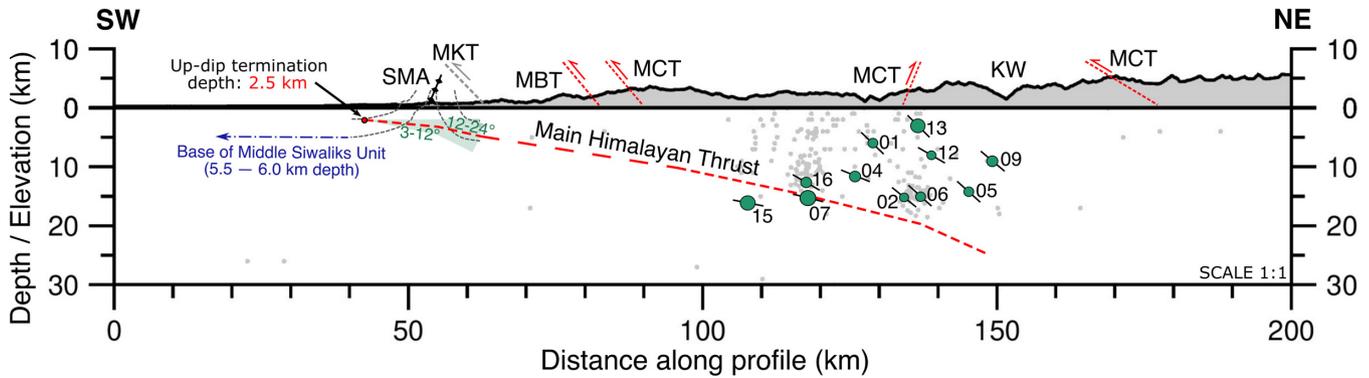
Figure 9. Cross-section taken along A–A' in Fig. 2, showing the downdip structure of the Main Himalayan Thrust (MHT) across Jammu and Kashmir in the NW Himalaya. The SMA fold structure from the balanced cross-sections is shown by light-grey lines, with the inferred base of the Middle Siwaliks in blue. Waveform-modelled earthquakes from this study and Baranowski *et al.* (1984) are represented as the SE-dipping nodal plane (black solid lines) with a green circle scaled in diameter by the earthquake seismic moment. For earthquakes where it was not possible to invert for a focal mechanism, we began by using a representative focal mechanism based on fault plane solutions of neighbouring earthquakes after Molnar & Lyon-Caen (1989), Mitra *et al.* (2014) and Paul *et al.* (2018) who previously waveform modelled a select number of moderate-magnitude earthquakes in the region. We then varied the dip of the nodal planes to investigate which range was compatible with the polarity of the direct *P*-wave arrivals (see Supporting Information for an analysis of each earthquake's waveform solution). Earthquakes from Paul *et al.* (2018) and Agrawal *et al.* (in review) are shown as light grey dots. Faults are labelled as in Fig. 2. Also shown is our inferred fault geometry (in red), as described in the text.

(e.g. the presence of foreland basins). Such work can also explore the wave-propagation effects which control the amplitude and duration of the ground motions (Bowden & Tsai 2017; O'Kane & Copley 2021), which is fundamental for understanding seismic hazard variations on regional scales.

5.1 Methodology

We used the SW4 (Seismic Waves, 4th Order) finite-difference code (Petersson & Sjögreen 2017) to solve the viscoelastic wave equation with fourth-order accuracy in time and space for various earthquake rupture configurations in the region (Petersson & Sjögreen 2012, 2015). This method eliminates artificial reflections from far-field boundaries by using a damping layer on all model boundaries except for the free surface (Petersson & Sjögreen 2014). It also allows for the use of a 3-D material model, which is beneficial for accurately modelling the heterogeneity in the crust (Petersson & Sjögreen 2012).

SW4's ability to simulate earthquake ground motions at a regional scale and at frequencies relevant to urban infrastructure (∼0.1–10 Hz, Parajuli & Kiyono 2015; Moisidi *et al.* 2018) make it an appropriate method for use in our study (Petersson & Sjögreen 2012, 2015; McCallen *et al.* 2021). The method has been widely used in site-specific studies (e.g. Dreger *et al.* 2015; Pitarka *et al.* 2016; Rodgers *et al.* 2018, 2019b), where the modelled ground motions were consistent with observations and other ground-motion models (Rodgers *et al.* 2019a).

5.2 Model setup

The model setup was designed to replicate the present-day configuration of the NW Himalayan range front and its adjacent foreland. The computational domain is 100 km wide in the along-strike direction, 150 km in across-strike length, and 30 km deep. The model domain was discretized into a grid with a spacing of 100 m, which is fine enough to resolve all frequencies in the range 0.015–1.5 Hz (Petersson & Sjögreen 2012, 2015). In this paper, we concentrate exclusively on the large-scale (regional) controls that the fault geometry and subsurface structure have on the earthquake-induced

ground motions. It is known that the shallow velocity structure (particularly the average shear wave velocity for the top 30 m, which is commonly known as $V_s 30$) can have a large effect on the amplification of ground shaking (Anderson *et al.* 1996; Catchings & Lee 1996; Boore & Joyner 1997), as discussed below. However, these smaller-scale, short-period effects from the shallow geology will be superimposed on the larger-scale geometrical effects which control the characteristics of the waves entering the near-surface, which we focus on in this paper.

The material properties of the model domain [V_p (*P*-wave seismic velocity), V_s (*S*-wave seismic velocity), Q_p (*P*-wave seismic attenuation), Q_s (*S*-wave seismic attenuation) and ρ (density)] were designed to represent the major geological components of the NW Himalaya and its foreland basin. We generated a depth-variable material structure for our model by averaging the 1-D velocity, attenuation and density models for three discrete regions across-strike of the NW Himalayan range front: the Indian Crust (Dube *et al.* 1973; Bhattacharya 1991; Gaur & Priestley 1997; Singh *et al.* 1999; Cattin *et al.* 2001; Rai *et al.* 2003; Mitra *et al.* 2006; Shearer *et al.* 2006; Hetényi *et al.* 2007; Srinagesh *et al.* 2011; Agrawal *et al.* in review), the Lesser and Higher Himalaya (Ni *et al.* 1991; Hetényi *et al.* 2007; Mahesh *et al.* 2013; Sharma *et al.* 2014; Tiwari *et al.* 2015; Agrawal *et al.* in review; Bera *et al.* in review) and the foreland basin sediments (Chun 1986; Bhattacharya 1992; Cattin *et al.* 2001; Hetényi *et al.* 2006; Suresh *et al.* 2008; Mitra *et al.* 2011; Chen & Wei 2019). Each of the published profiles and our resultant depth-variable material model is illustrated in Fig. S21. A cross-section through our material model for V_p is shown in Fig. 11(e). The material properties are homogeneous along-strike of the computational domain. The material grids for V_s, Q_p, Q_s and ρ are presented in Fig. S22. The model comprises a northward-dipping 4.5–6.5 km deep Indus foreland basin (Bhattacharya 1992; Suresh *et al.* 2008; Mitra *et al.* 2011) overlying Indian basement material (see Fig. 11). This underlying Indian basement material is also used for the velocity structure beneath the modelled thrust fault, with the Himalayan velocity model in the hanging wall.

We simulated thrust-faulting earthquakes along our newly defined MHT geometry, constructed from the results of Sections 2, 3 and 4. Each simulation recorded the wavefield at synthetic receiver
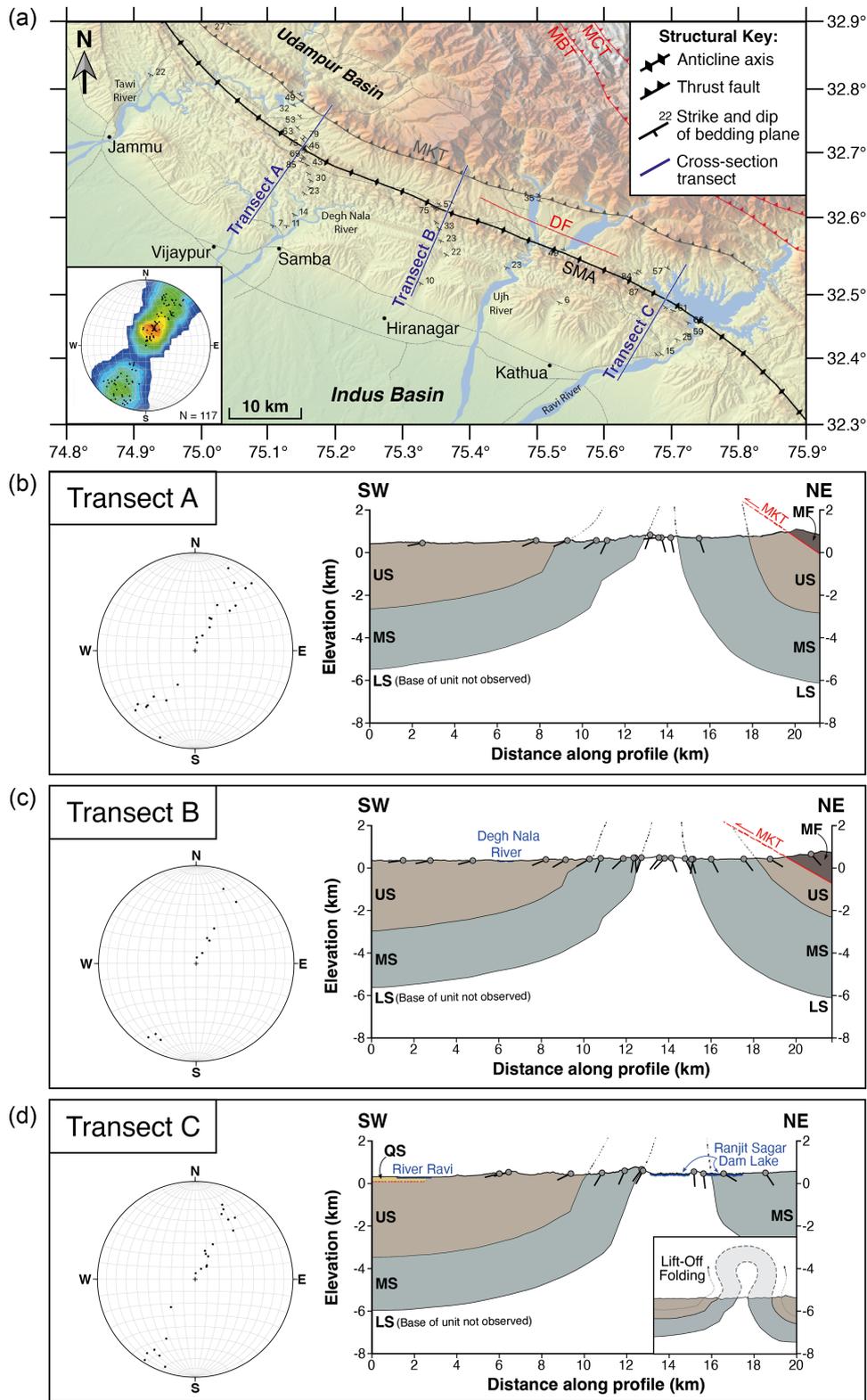
Figure 10. Structure of the Surin Mastgarh Anticline (SMA). (a) Topographic map of the SMA showing three transects where we collected structural data across the fold. Faults have been traced after Gavillot *et al.* (2016) and our field observations with labels: DF, Darung Fault; MBT, Main Boundary Thrust; MCT, Main Central Thrust; MKT, Mandili Kishanpur Thrust. An inset equal-area lower hemisphere stereographic projection illustrates the overall structure of the fold with Kamb contours plotted (after Kamb 1959) every tenth of a standard deviation, showing a significant cluster in the poles to bedding plane points. Panels (b), (c) and (d) show estimated cross-sections and stereographic projections of the poles to bedding collected across transects A, B and C, respectively. The geological unit labels are as follows: US, Upper Siwaliks; MS, Middle Siwaliks; LS, Lower Siwaliks; MF, Murree Formation; QS, Quaternary Sediments. The inset in (d) illustrates a simplified lift-off fold geometry for the SMA, prior to erosion [redrawn from Mitra (2003)].
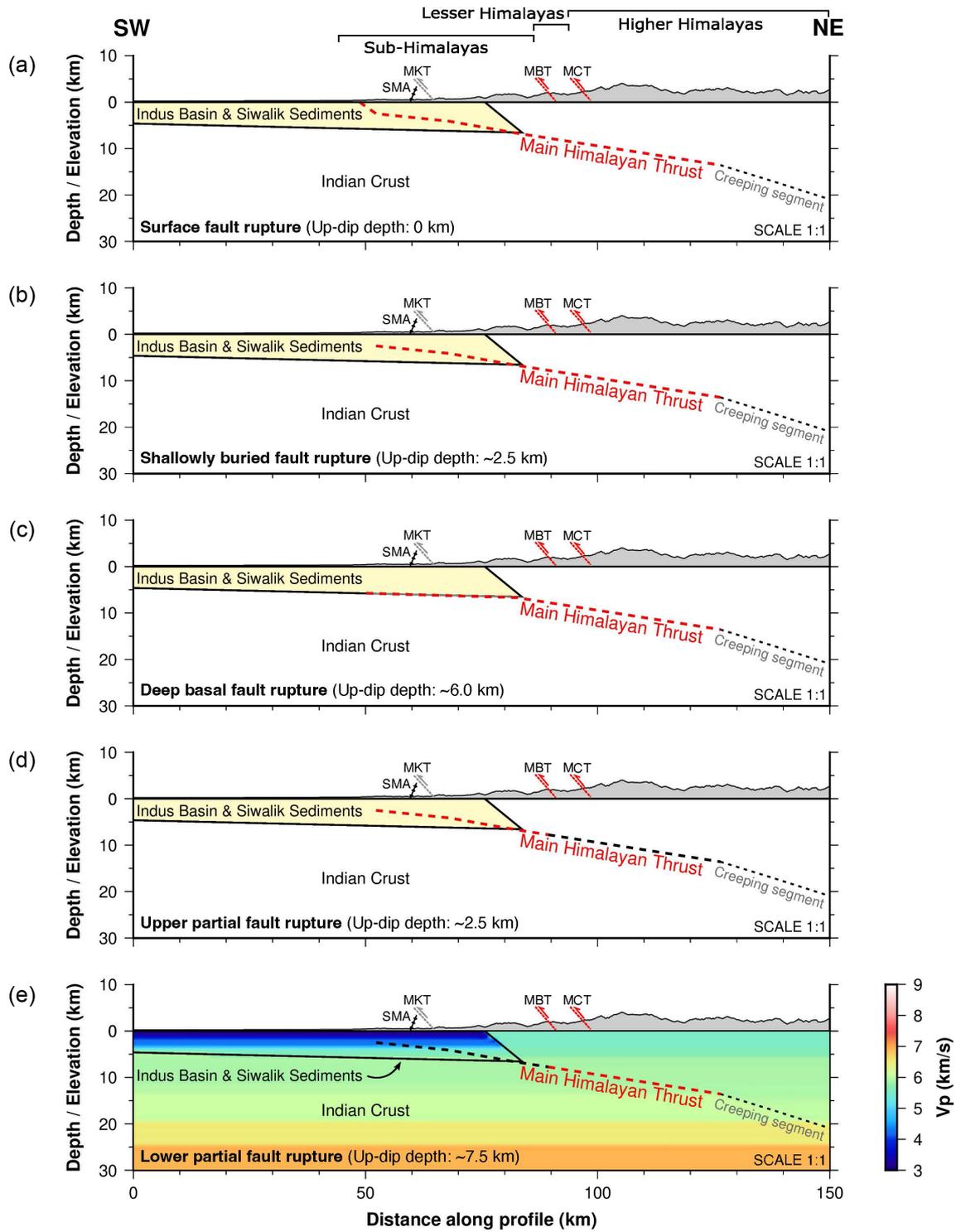
Figure 11. Configurations of the thrust geometry used in the ground-motion modelling. (a), (b) and (c) illustrate cross-sections through the model setups for ground-motion simulations with a surface-rupturing (e.g. Nepal), shallowly-buried (e.g. NW India) and deep fault (e.g. eastern Pakistan) geometry. Panels (d) and (e) show cross-sections through the model setups for partial ruptures of the upper (e.g. potential post-Gorkha earthquake) and lower portion of the fault (e.g. 2015 Gorkha earthquake). The ruptured portions of the Main Himalayan Thrust are shown in red and the Indus Basin in yellow. The topography is shown in grey, although the topography itself is not included in our models. All other labels are the same as in Fig. 2. Panel (e) illustrates a cross-section through the material model we used for V_p. The grids for the other material properties (V_s, Q_p, Q_s and ρ) used in our model are presented in Fig. S22.

stations that were placed at 1 km intervals, in a line running across-strike through the centre of the model domain. The moment release and rupture process on the MHT were parameterised as follows. The spatial distribution of moment release on the MHT was approximated by placing subsources spaced 100 m apart along-strike and downdip. To calculate the moment release at each of these subsources, we defined a slip distribution on the MHT and distributed the moment release between the subsources. The slip distribution was taken to have a peak slip of 8 m in the centre of the fault, and was linearly tapered towards the margins of the rupture area forming an elliptical slip patch. The peak slip of 8 m was imposed to replicate the slip deficit accumulated in the NW Himalaya since the last major earthquake (Schiffman *et al.* 2013; Bilham 2019; Jade *et al.* 2020). At each subsource a Gaussian source–time function was used, and we set the angular frequency of each subsource to ∼3.77 Hz, which equates to a fundamental frequency (f_0) of 0.6 Hz (Sjögreen & Petersson 2012). The angular frequency was selected such that all frequencies in the range of 0.015–1.5 Hz could be simulated.

Rupture propagation was simulated by setting the time of moment release at each subsource. We defined the rupture to initiate at the bottom corner of the locked patch of the MHT and rupture updip and along-strike at a velocity of 2.5 km s^{-1}, based on models of past continental thrust-faulting earthquakes (Wen *et al.* 2012; Avouac *et al.* 2015; Yagi & Okuwaki 2015; Lay *et al.* 2017). Deeper sections of the MHT are thought to be creeping aseismically (Bollinger *et al.* 2004), which limits the downdip extent of the rupture area. In Jammu, the cluster of earthquakes ∼100 km NE of the range front are thought to represent the locked-to-creeping transition along the MHT, as discussed above, suggesting that the available rupture area has a 75–80 km downdip width. The along-strike length of the rupture is constrained to be equal to the downdip width (Scholz 1982). This geometry is consistent with the <100 km along-strike length of the SMA being underlain by a coherent fault plane that breaks in single events. The total resulting moment magnitude of the synthetic earthquakes varies depending on the imposed geometry of the shallow part of the faulting, as described below.

In each simulation, the velocity structure, rupture process and model domain remain the same. What we vary between simulations is the geometry of the shallow part of the thrust fault, and the depth-extent of the thrust fault that ruptures. We calculate the ground motions from five different thrust fault configurations, to explore the effects of fault geometry on the resulting ground motions. In Model 1 (Fig. 11a) the shallow thrust has a geometry similar to that seen in the Nepal Himalaya, where a steeper-dipping splay connects the fault at depth to the surface (Brunel 1986; Schelling 1992; Mugnier *et al.* 1999). In Model 2 (Fig. 11b) the splay connecting the thrust to the surface is not present, and fault slip terminates at 2.5 km depth, as we suggest is the case in the J&K region. In Model 3 (Fig. 11c) the thrust ruptures along the sediment-basement interface, replicating the geometry observed in places where the faulting is deeper (e.g. as event 03 on Fig. 2 suggests is the case in eastern Pakistan). Model 4 (Fig. 11d) was designed to reflect a rupture where only the shallowest part of the thrust ruptures, and Model 5 (Fig. 11e) represents only the deepest portion of the thrust rupturing. Model 5 therefore represents a 'Gorkha-style' rupture, and Model 4 is equivalent to an earthquake on the remaining locked portion of the MHT, updip of the 2015 Gorkha earthquake (e.g. Wesnousky *et al.* 2017a). The corresponding moment magnitudes of the synthetic earthquakes are $M_w = 7.7$, 7.7, 7.7, 7.4 and 7.5 for Models 1–5, respectively. The moment magnitudes vary slightly between models to reflect the downdip width of the fault, although

all other dimensions are kept the same. In the following section, we describe the simulated ground motions for each of these different rupture geometries.

It is important to consider the frequency content of our modelled waveforms and the shallow subsurface structure when interpreting the model results. We will present below the peak ground velocity (PGV) produced by our models. The peak PGV values in recordings of natural earthquakes generally occur at frequencies ≤1 Hz (Boore 2001; Frankel *et al.* 2002; Frankel 2009; Takai *et al.* 2016), so would be resolvable in our models. The dominant frequencies produced by our model setup are similar to those of past Himalayan earthquakes, such as the 0.15–0.70 Hz observed in the 2015 Gorkha earthquake (Galetzka *et al.* 2015; Tallett-Williams *et al.* 2016; Rajaure *et al.* 2017; Chen & Wei 2019). However, our computational domain does not allow us to model variations in the shallow velocity structure, which can have an important effect on the ground motions. Our models can, however, demonstrate the larger-scale wave propagation effects that control the nature of the seismic energy that enters the subsurface. The minimum *S*-wave velocity in our modelled basin is 1700 m s^{-1}. Shallow low-velocity layers would result in ground motion amplification at those sites (Anderson *et al.* 1996; Catchings & Lee 1996; Boore & Joyner 1997). However, we do not have detailed information on the shallow subsurface structure for our study region, and the size of our computational domain prevents us from implementing short-wavelength, shallow velocity variations. Any such shallow velocity variations would have the same effects on all of the models we discuss in this paper, which use the same velocity structure (see Figs S21 and S22). Therefore, these models should be interpreted as providing an understanding of the relative PGV values for a range of different fault geometries, rather than being accurate assessments of the absolute values that may be produced by an earthquake in the region.

The peak ground acceleration (PGA) produced by earthquakes can be affected by energy at frequencies larger than those we model here. Such a situation will be relevant when an earthquake produces significant high-frequency radiation (such as in the case of the 1994 Northridge buried thrust-faulting earthquake, Finn *et al.* 1995; Field *et al.* 1998), and in near-source locations where the high frequencies have not yet been preferentially attenuated. We focus on the more well-resolved PGV results in this paper, which some studies suggest have the closest correlation with intensity measures and damage statistics (Schenk *et al.* 1990; Wald *et al.* 1999; Wu *et al.* 2003). However, when comparing our models to observations from past earthquakes, we make use of the PGA ground motion metric, and in these cases, we use the PGAs within our modelled frequency band.

5.3 Model results

Fig. 12 shows the permanent ground displacement and absolute PGV that would result from Models 1, 2 and 3 in which we varied the geometry of the very shallowest part of the thrust (Fig. 12a). All three models have low PGV where the fault ruptures the deepest part of the thrust, with a progressive increase in the PGV as the fault depth decreases between distances of 150 and 75 km across-strike. At distances <75 km across-strike, near the deepest part of the foreland basin, the PGVs between the models with different rupture scenarios begin to deviate significantly. The model in which the fault ruptures the surface produces the highest PGVs of the three (Figs 11a–c) with peak velocities in excess of >5 ms^{-1}.

The modelled PGV values are consistent with observations from past thrust earthquakes of a similar magnitude. For example,
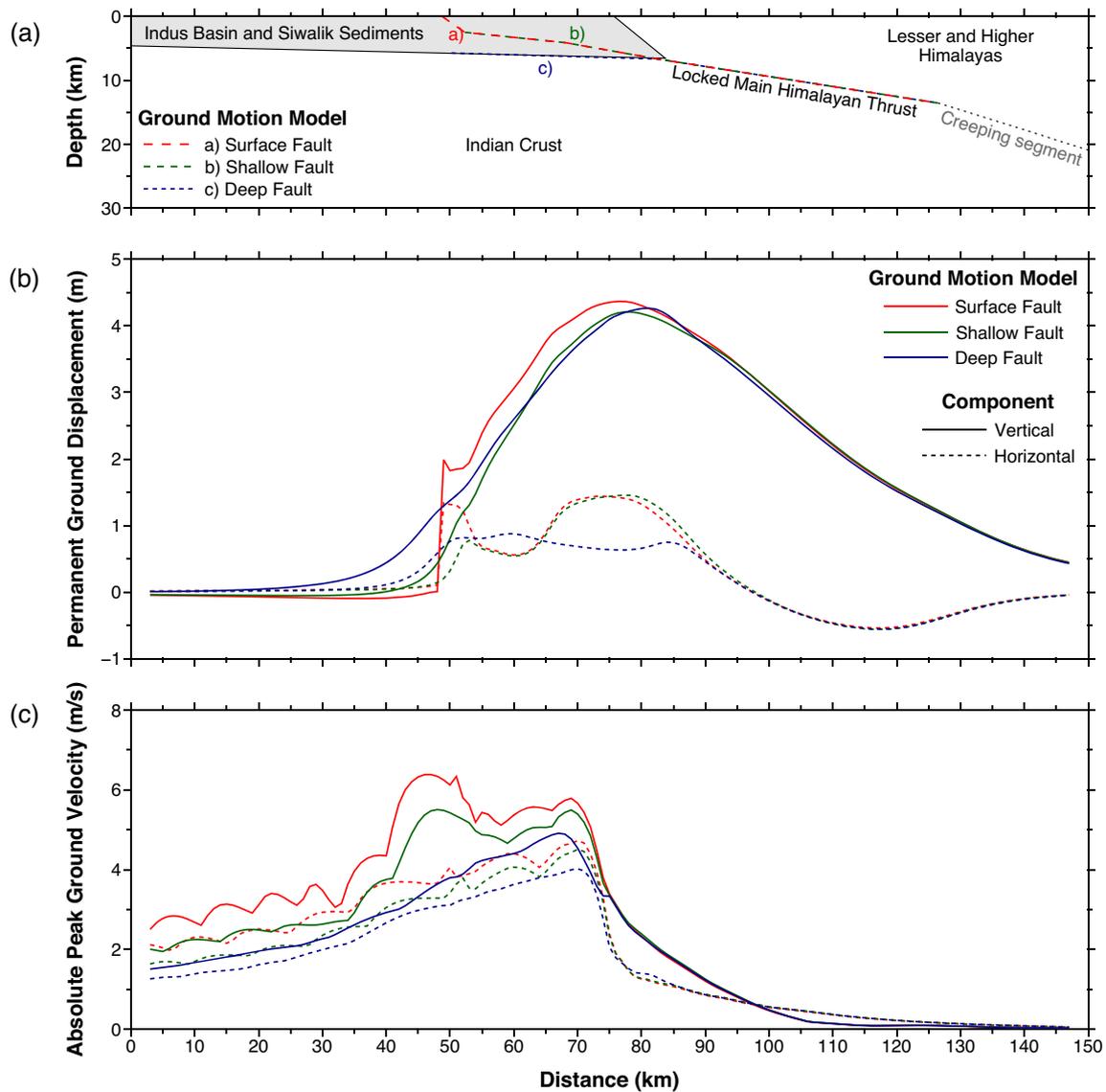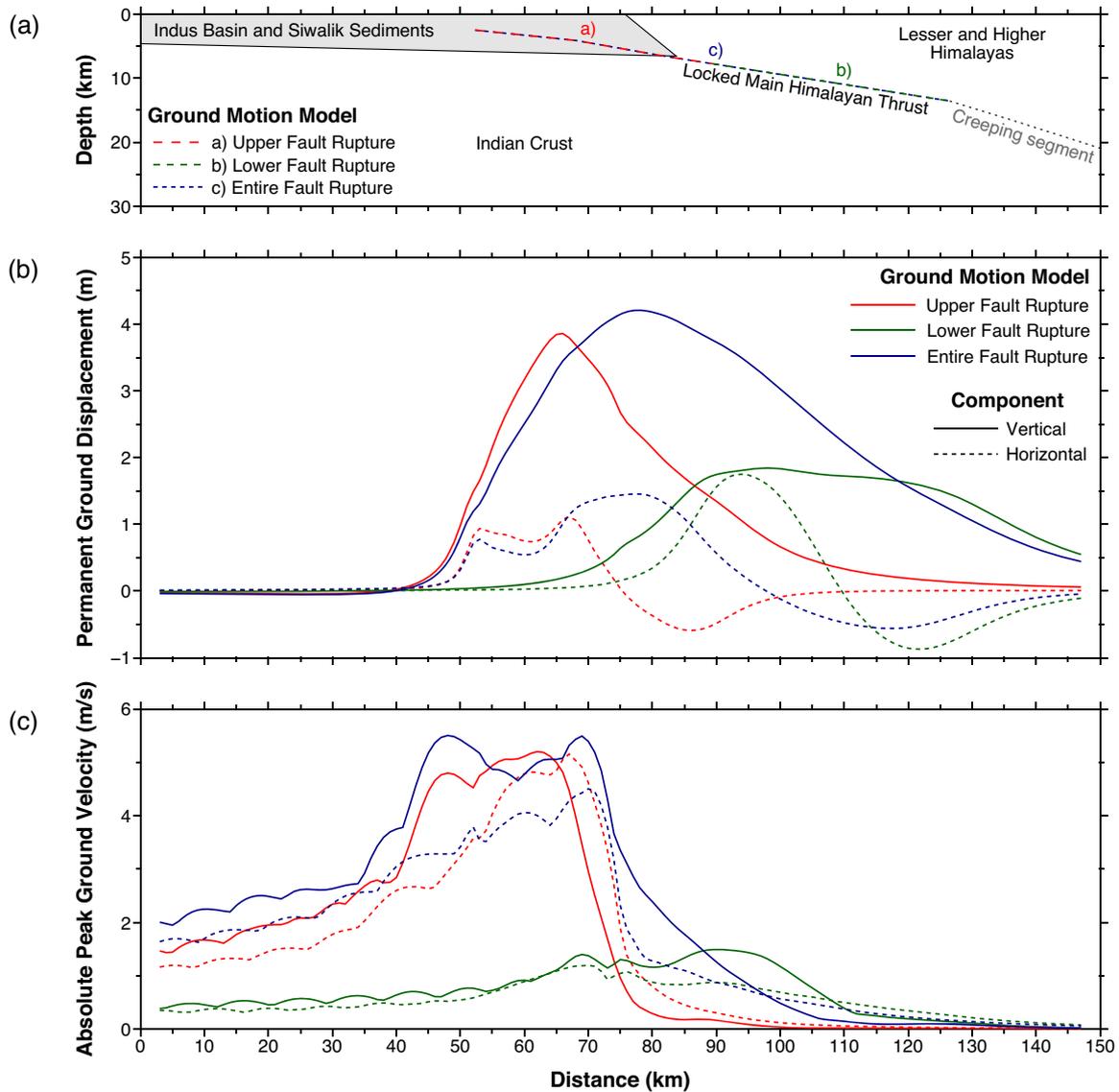
Figure 12. Calculated ground motions as a function of distance across-strike for models with three different shallow thrust geometries. (a) Model cross-section illustrating the three source geometries [surface-rupturing fault (e.g. Nepal), shallowly-buried fault (e.g. Jammu, NW India) and deep basal fault (e.g. eastern Pakistan)]. Panels (b) and (c) show permanent ground displacement and absolute peak ground velocity, respectively, along a line running across-strike through the centre of the model domain. The minimum S-wave velocity in our modelled basin is 1700 ms^{-1} and the full velocity structure is illustrated in Figs S21 and S22.

Lu *et al.* (2010) showed that the surface-rupturing 1999 M_w 7.6 Chi-Chi, Taiwan earthquake resulted in PGV values of up to ∼3 ms^{-1}, whilst buried-fault earthquakes such as the 1978 M_w 7.4 Tabas, Iran earthquake generated lower PGVs of up to ∼1.2 ms^{-1}. Similarly, Lu *et al.* (2010) recorded PGVs in the range of ∼0.2–1.4 m s^{-1} for the 2008 M_w 7.9 Wenchuan earthquake. Although lower in magnitude, the 1994 M_w 6.7 Northridge earthquake produced PGV values of ∼1.5 m s^{-1}, highlighting the possibility that the values from the larger events may underestimate the true maximums due to the sparsity of recordings (Suzuki & Iervolino 2017). The lateral variability in the measurements from each of these events, at a given distance from the fault, is likely to be related to lateral contrasts in the shallow velocity structure, which as discussed above is not included in our models. However, the general agreement in our modelled PGV values and those from past thrust events show that our models are sufficiently close to observations that they can be effectively used to

examine the controls that the fault geometries described above can play on the ground motions, as an intercomparison of the relative values between the models.

As discussed above, we are only able to measure the PGA resulting from waves within our resolved frequency band, which can underestimate the true value for cases where sites experience plentiful high-frequency shaking. However, our estimated values in the range of ∼3–15 m s^{-2} within ∼20 km distance from the ruptures in Models 1, 2 and 3 (see Figs 11a–c), are similar to recordings of large thrust earthquakes, such as the 2008 Wenchuan earthquake where PGAs were recorded in the range of 4–10 m s^{-2} (Wen *et al.* 2014) and the 1971 San Fernando earthquake where PGAs as high as 12.3 m s^{-2} were recorded (Trifunac 1972). This agreement may suggest that either the spectra produced by large events are dominated by frequencies ≤1.5 Hz (as in our model setup), or that the higher frequencies are rapidly attenuated. Our model results are

Figure 13. Peak ground motions as a function of distance across-strike for models with varying rupture geometries. (a) Model cross-section illustrating the three different fault rupture geometries [upper fault (potential post-Gorkha earthquake), lower fault (e.g. 2015 Gorkha earthquake) and entire fault (great Himalayan earthquakes with $M_w > 8$)]. (b) and (c) show permanent ground displacement and absolute peak ground velocity, respectively, along a line running across-strike through the centre of the model domain. The minimum S-wave velocity in our modelled basin is 1700 ms^{-1} and the full velocity structure is illustrated in Figs S21 and S22.

within a similar range to those of the previous models of Harbindu *et al.* (2014), who calculate ground motion model PGAs on the order of 1–10 ms^{-2} for the neighbouring Garhwal Himalaya, following the empirical rules of Abrahamson & Litehiser (1989), Singh *et al.* (1996), Abrahamson & Silva (1997), Boore & Atkinson (2008) and Sharma *et al.* (2009).

The surface-rupturing earthquake (Model 1) produces PGVs that are ∼18 per cent higher than those generated by the shallow fault model (Model 2). Most notably, the surface-rupturing earthquake scenario (Model 1) produces almost 1 ms^{-1} higher PGVs than the deep fault scenario (Model 3), equating to a ∼20 per cent higher PGV resulting from an earthquake with a ∼10 per cent lower moment magnitude. Therefore, we can deduce that the shallow fault geometry has a greater effect on the ground motions than the differences in earthquake magnitude between the scenarios, and our

results illustrate that minor variations in the shallow fault geometry can have a large effect on the ground motions produced.

The high PGVs from these shallow thrust ruptures are a result of a combination of factors. The most influential factor is the source depth, in addition to the fault dip (O'Kane & Copley 2021). The shallow part of the thrust also cross-cuts the foreland basin sediments, which amplify ground motions (Bard & Bouchon 1985; Rial *et al.* 1992; Joyner 2000; Meza-Fajardo *et al.* 2016; Rajaure *et al.* 2017). Previous results (O'Kane & Copley 2021) show that the overall shape and amplitude of the PGV curves are governed by the source geometry (particularly the depth), and the basin depth and geometry. The small-wavelength (<10 km) undulations in PGV within the basin are a result of body-wave resonance.

The results shown in Fig. 12 demonstrate that, although the differences in the three fault geometries we have tested are relatively

minor, they have significant impacts on the calculated ground motions. In particular, whether the updip section of the fault is subhorizontal at depth (as in eastern Pakistan, Jouanne *et al.* 2020), or terminates at 2.5 km depth (as in J&K), or ruptures to the surface (as observed further east along the Himalaya; Wesnousky *et al.* 2017a), can change the resulting surface ground motions significantly. This result highlights the importance of accurately determining subsurface fault geometries when conducting hazard assessments.

Fig. 13 shows the permanent ground displacement and peak ground velocity that would result from Models 2, 4 and 5 in which we varied the area of the fault that ruptures. These calculations were conducted to estimate the differences in ground motion that would result from a complete or partial rupture of the thrust, and were motivated by the observation that the 2015 Gorkha earthquake only ruptured the bottom half of the locked portion of the MHT (Galetzka *et al.* 2015).

The most striking result from these calculations is the comparatively small PGVs observed for the models in which only the lower portion of the fault breaks (Fig. 13). For example, the PGVs for earthquakes that rupture either the whole fault or just the shallow part of the fault are both relatively similar in amplitude directly above the rupture with PGVs of >5 m s^{-1}. The PGVs generated by the lower-fault rupture reach a maximum of ~ 1.5 m s^{-1}, similar to the ground motions reported by Hough *et al.* (2016) following the 2015 Gorkha earthquake, where PGV values of ~ 0.3–1.1 m s^{-1} in Nepal were recorded, reducing to <0.12 m s^{-1} for Indian sites situated >100 km from the fault that ruptured. These simple calculations demonstrate the potentially hazardous ground motions that would be generated if the upper, and most likely locked (Ingleby *et al.* 2020), part of the MHT in Nepal was to break in the future (Fig. 13). Although a more serious scenario would be if a M_w 8 earthquake were to rupture the whole fault, from the base of the locked zone to the surface, the PGVs generated by only a shallow rupture of the MHT are similar in amplitude and still pose a severe hazard.

In the preceding analysis, we have assumed the rupture of a single along-strike segment of the fault. The worst-case scenario would be, however, if the entire fault segment beneath Jammu were to rupture along with other fault segments along-strike (such as those that ruptured to the southeast in the 1905 Kangra earthquake and/or to the northwest during the 1555 Kashmir earthquake). These scenarios would result in a higher-magnitude event, possibly more similar to the 1505 event in western Nepal, which may have been closer to magnitude 9 (Bilham 2019). However, in this manuscript we limit ourselves to analysing scenarios in which only the fault segment underlying the SMA ruptures.

5.4 Implications for seismic hazard

Overall, our results emphasise the critical role that the fault geometry has on the ground motions produced by large thrust earthquakes, meaning that it is important that we better constrain the shallow thrust structure across the whole Himalayan range front, and on mountain range fronts in general. Our results also indicate that not only does the source depth play an important role in controlling earthquake ground motions at a given location, but also the underlying velocity structure and site conditions, such as the subsurface geology (i.e. basin sediments or crystalline basement) and its distance from the earthquake-generating fault. The ground motions we have modelled are significantly lower in the Lesser and Higher

Himalayas than in the foreland basin, due to the material which makes up the crust in those regions. The model results demonstrate that cities built on the Siwalik foothills or Himalayan foreland are at risk of experiencing higher ground motions from earthquakes than those in the mountainous regions built on bedrock further north.

The Himalaya is one of the most rapidly deforming mountain ranges in the world, and the structures that accommodate the shortening change significantly over time. Therefore, what may appear to be the most obvious deformation structure at the surface, may in fact hide the current fault geometry (e.g. the SMA in Jammu now appears to be inactive and cut by an active thrust at depth). It is therefore important that we carefully study not just the structural geology of these regions, but also the Holocene–Pleistocene geomorphology to determine the most recent configuration of deformation. In this way, we can more accurately determine the possible fault geometries at depth, which is critical for estimating the seismic hazard posed by large thrust-faulting earthquakes.

6 CONCLUSIONS

We have used seismology and geomorphology to constrain the downdip structure of the Main Himalayan Thrust in the NW Himalayan seismic gap near Jammu. We find that the MHT does not reach the surface in this region, but terminates at ~ 2.5 km depth beneath the Surin Mastgarh Anticline, which is the main expression of shortening at the surface. We have also been able to document the fault geometry at depth, as far as the likely downdip limit of brittle deformation. Seismic-wave-propagation simulations using this newly defined fault geometry, and the equivalent shallow fault geometry from elsewhere along the Himalayan arc, highlight the importance of the shallow thrust structure on the predicted ground motions. Faults that rupture to the surface can generate peak ground velocities that are ~ 20 per cent larger than those where the rupture remains buried within the foreland basin deposits. Similarly, we find that rupture along the updip portion of the MHT will produce >3 times higher peak ground velocities than rupture along its lower portion. Our results indicate that accurate constraints on the shallow geometry of thrust faults around the margins of mountain ranges are required for estimating seismic hazard in these critically-exposed regions.

DATA AVAILABILITY

Digital elevation data was sourced from the Shuttle Radar Topography Mission (which can be freely downloaded from http://www2.jpl.nasa.gov/srtm/), and the TanDEM-X Mission, which we sourced from the German Aerospace Center (DLR) (proposal number DEM-GEOL1445). GPS velocities were acquired from a local NW Himalaya study (Kundu *et al.* 2014) and global Strain Rate Model (Kreemer *et al.* 2014), available for download from https://storage.globalquakemodel.org/what/seismic-hazard/strain-rate-model/. Earthquake data was sourced from individual studies referenced in the manuscript, in addition to global catalogues: (1) Centroid moment tensor data was downloaded from https://www.globalcmt.org/, (2) ISC-EHB data was acquired from http://www.isc.ac.uk/isc-ehb/, (3) Waveform-modelled earthquake source parameters were downloaded from https://comet.nerc.ac.uk/gwfm_catalogue/ and (4) Earthquake seismogram data was acquired from IRIS at https://ds.iris.edu/wilber3/find_event/. The SW4 finite-difference code, developed at the Lawrence Livermore National Laboratory, is available to download from www.geodynamics.org/cig/software/sw4/. All figures have been produced using Generic Mapping Tools v6 (Wessel *et al.* 2019).

REFERENCES

Abrahamson, N.A. & Litehiser, J.J., 1989. Attenuation of vertical peak acceleration, *Bull. seism. Soc. Am.,* **79**(3), 549–580.

Abrahamson, N.A. & Silva, W.J., 1997. Empirical response spectral attenuation relations for shallow crustal earthquakes, *Seismol. Res. Lett.,* **68**(1), 94–109.

Ader, T. *et al.*, 2012. Convergence rate across the Nepal Himalaya and interseismic coupling on the Main Himalayan Thrust: implications for seismic hazard, *J. geophys. Res.,* **117**(4), 1–16.

Agrawal, H., Mitra, S., Sharma, S., Wanchoo, S.K., Priestley, K. & Haberland, C., in review. 3D velocity structure and earthquakes beneath Jammu and Kashmir Himalaya, *Geophys. Res. Lett*.

Ainscoe, E.A., Elliott, J.R., Copley, A., Craig, T.J., Li, T., Parsons, B.E. & Walker, R.T., 2017. Blind thrusting, surface folding, and the development of geological structure in the Mw 6.3 2015 Pishan (China) earthquake, *J. geophys. Res.,* **122**(11), 9359–9382.

Allmendinger, R.W. & Shaw, J.H., 2000. Estimation of fault propagation distance from fold shape: implications for earthquake hazard assessment, *Geology,* **28**(12), 1099–1102.

Ambraseys, N. & Bilham, R., 2000. A note on the Kangra $M_s = 7.8$ earthquake of 4 April 1905, *Curr. Sci.,* **79**(1), 45–50.

Ambraseys, N. & Jackson, J., 2003. A note on early earthquakes in northern India and southern Tibet, *JSTOR,* **84**(4), 570–582.

Anderson, J.G., Lee, Y., Zeng, Y. & Day, S., 1996. Control of strong motion by the upper 30 meters, *Bull. seism. Soc. Am.,* **86**(6), 1749–1759.

Aravind, A., Mishra, R.L., Jagtap, S., Jayangondaperumal, R., Thakur, V.C., Pant, C.C. & Joevivek, V., 2022. Detachment folding, growth mechanism and seismic potential in the Jammu Sub-Himalaya, *J. Struct. Geol.,* **155**(January), 104514, doi:10.1016/j.jsg.2022.104514.

Avouac, J.P., Meng, L., Wei, S., Wang, T. & Ampuero, J.P., 2015. Lower edge of locked Main Himalayan Thrust unzipped by the 2015 Gorkha earthquake, *Nat. Geosci.,* **8**(9), 708–711.

Baranowski, J., Armbruster, J. & Seeber, L., 1984. Focal depths and fault plane solutions of earthquakes and active tectonics of the Himalaya, *J. geophys. Res.,* **89**(B8), 6918–6928.

Bard, P.Y. & Bouchon, M., 1985. The two-dimensional resonance of sediment-filled valleys, *Bull. seism. Soc. Am.,* **75**(2), 519–541.

Bera, A., Mitra, S., Wanchoo, S.K. & Priestley, K., in review. Seismic attenuation tomography of the Jammu and Kashmir Himalaya, *J. geophys. Res.*

Bhattacharya, S.N., 1991. Surface wave and lithospheric structure across the northwestern part of the Indian Peninsula, *Pure appl. Geophys.,* **135**(1), 53–59.

Bhattacharya, S.N., 1992. Crustal and upper mantle velocity structure of India from surface wave dispersion, *Curr. Sci.,* **62**(1–2), 94–100.

Bilham, R., 2019. Himalayan earthquakes: a review of historical seismicity and early 21st century slip potential, *Geol. Soc. Spec. Publ.,* **483**(1), 423–482.

Bollinger, L., Avouac, J.P., Cattin, R. & Pandey, M.R., 2004. Stress buildup in the Himalaya, *J. geophys. Res.,* **109**(11), 1–8.

Bollinger, L. *et al.*, 2014. Estimating the return times of great Himalayan earthquakes in eastern Nepal: evidence from the Patu and Bardibas strands of the Main Frontal Thrust, *J. geophys. Res.,* **119**, 7123–7163.

Boore, D.M., 2001. Effect of baseline corrections on displacements and response spectra for several recordings of the 1999 Chi-Chi, Taiwan, earthquake, *Bull. seism. Soc. Am.,* **91**(5), 1199–1211.

Boore, D.M. & Atkinson, G.M., 2008. Ground-motion prediction equations for the average horizontal component of PGA, PGV, and 5 per cent-damped PSA at spectral periods between 0.01 s and 10.0 s, *Earthq. Spectra,* **24**(1), 99–138.

Boore, D.M. & Joyner, W.B., 1997. Site amplifications for generic rock sites, *Bull. seism. Soc. Am.,* **87**(2), 327–341.

Bowden, D.C. & Tsai, V.C., 2017. Earthquake ground motion amplification for surface waves, *Geophys. Res. Lett.,* **44**(1), 121–127.

Brunel, M., 1986. Ductile thrusting in the Himalayas: shear sense criteria and stretching lineations, *Tectonics,* **5**(2), 247–265.

Burbank, D.W., Beck, R.A., Mulder, T., Yin, A. & Harrison, T.M., 1996. The Himalayan foreland basin, in *The Tectonic Evolution of Asia, Series: World and Regional Geology,* Chapter 9, pp. 149–190, Yin, A. & Harrison, T.M., Cambridge Univ. Press.

Catchings, R.D. & Lee, W.H., 1996. Shallow velocity structure and Poisson's ratio at the Tarzana, California, strong-motion accelerometer site, *Bull. seism. Soc. Am.,* **86**(6), 1704–1713.

Cattin, R., Martelet, G., Henry, P., Avouac, J.P., Diament, M. & Shakya, T.R., 2001. Gravity anomalies, crustal structure and thermo-mechanical support of the Himalaya of Central Nepal, *Geophys. J. Int.,* **147**(2), 381–392.

Chapman, C.H., 1978. A new method for computing synthetic seismograms, *Geophys. J. R. astr. Soc.,* **54**(3), 481–518.

Chapman, C.H., Jen-Yi, C., Lyness, D.G. & Doornbos, D.J., 1988. The WKBJ seismogram algorithm, in *Seismological Algorithms: Computational Methods and Computer Programs,* pp. 47–74, ed. Doornbos., D.J., Academic Press.

Chen, M. & Wei, S., 2019. The 2015 Gorkha, Nepal, earthquake sequence: II. Broadband simulation of ground motion in Kathmandu, *Bull. seism. Soc. Am.,* **109**(2), 672–687.

Chen, W.P. & Molnar, P., 1983. Focal depths of intracontinental and intraplate earthquakes and their implications for the thermal and mechanical properties of the lithosphere, *J. geophys. Res.,* **88**, 4183–4214.

Christensen, D.H. & Ruff, L.J., 1985. Analysis of the trade-off between hypocentral depth and source time function and source time function, *Bull. seism. Soc. Am.,* **75**(6), 1637–1656.

Chun, K.Y., 1986. Crustal block of the western Ganga basin: a fragment of oceanic affinity?, *Bull. seism. Soc. Am.,* **76**(6), 1687–1698.

Craig, T.J., Copley, A. & Jackson, J., 2012. Thermal and tectonic consequences of India underthrusting Tibet, *Earth planet. Sci. Lett.,* **353-354,** 231–239.

Dal Zilio, L., Hetényi, G., Hubbard, J. & Bollinger, L., 2021. Building the Himalaya from tectonic to earthquake scales, *Nat. Rev. Earth Environ.,* **2,** 251–268.

DeCelles, P., Robinson, D., Quade, J., Ojha, T., Garzione, C.N., Copeland, P. & Upreti, B.N., 2001. Himalayan fold-thrust belt in western Nepal, *Tectonics,* **20**(4), 487–509.

Dey, S., Chauhan, N., Nath, D., Schaaf, N.W., Thiede, R.C. & Jain, V., 2021. Pleistocene-Holocene crustal deformation in the far-Western Himalaya, EarthArXiv. [Preprint.] June 25, 2021 [accessed 2021 July 01], doi:10.31223/X5GG77.v1.

Dreger, D.S., Huang, M.H., Rodgers, A., Taira, T. & Wooddell, K., 2015. Kinematic finite-source model for the 24 August 2014 South Napa, California, Earthquake from joint inversion of seismic, GPS, and InSAR data, *Seismol. Res. Lett.,* **86**(2A), 327–334.

Dube, R.K., Bhayana, J.C. & Chaudhury, H.M., 1973. Crustal structure of the Peninsular India, *Pure appl. Geophys.,* **109**(1), 1718–1727.

Dziewonski, A.M., Chou, T.A. & Woodhouse, J.H., 1981. Determination of earthquake source parameters from waveform data for studies of global and regional seismicity., *J. geophys. Res.,* **86**, 2825–2852.

Ekström, G., Nettles, M. & Dziewoński, A.M., 2012. The global CMT project 2004-2010: centroid-moment tensors for 13,017 earthquakes, *Phys. Earth planet. Inter.,* **200-201,** 1–9.

Emami, H., Vergés, J., Nalpas, T., Gillespie, P., Sharp, I., Karpuz, R., Blanc, E.P. & Goodarzi, M.G., 2010. Structure of the mountain front flexure along the Anaran anticline in the Pusht-e Kuh Arc (NW Zagros, Iran): insights from sand box models, *Geol. Soc. Spec. Publ.,* **330,** 155–178.

Emmerson, B., Jackson, J., McKenzie, D. & Priestley, K., 2006. Seismicity, structure and rheology of the lithosphere in the Lake Baikal region, *Geophys. J. Int.,* **167**(3), 1233–1272.

Engdahl, E.R., Hilst, R. V.D. & Buland, R., 1998. Global teleseismic earthquake relocation with improved travel times and procedures for depth determination, *Bull. seism. Soc. Am.,* **88**(3), 722–743.

Erslev, E.A., 1991. Trishear fault-propagation folding, *Geology,* **19**(6), 617–620.

Field, E.H., Zeng, Y., Johnson, P.A. & Beresnev, I.A., 1998. Nonlinear sediment response during the 1994 Northridge earthquake: observations and finite source simulations, *J. geophys. Res.,* **103**(B11), 26 869–26 883.

Finn, W.L., Ventura, C.E. & Schuster, N.D., 1995. Ground motions during the 1994 Northridge earthquake, *Can. J. Civil Eng.,* **22**(2), 300–315.

Frankel, A., 2009. A constant stress-drop model for producing broadband synthetic seismograms: comparison with the next generation attenuation relations, *Bull. seism. Soc. Am.,* **99**(2A), 664–680.

Frankel, A.D., Carver, D.L. & Williams, R.A., 2002. Nonlinear and linear site response and basin effects in Seattle for the M 6.8 Nisqually, Washington, Earthquake, *Bull. seism. Soc. Am.,* **92**(6), 2090–2109.

Futterman, W., 1962. Dispersive body waves, *J. geophys. Res.,* **67**(13), 5279–5291.

Galetzka, J. *et al.*, 2015. Slip pulse and resonance of the Kathmandu basin during the 2015 Gorkha earthquake, Nepal, *Science,* **349**(6252), 1091–1095.

Gaur, V.K. & Priestley, K., 1997. Shear wave velocity structure beneath the Archaean granites around Hyderabad, inferred from receiver function analysis, *Proc. Indian Acad. Sci.: Earth planet. Sci.,* **106**(1–2), 1–8.

Gavillot, Y., Meigs, A., Yule, D., Heermance, R., Rittenour, T., Madugo, C. & Malik, M., 2016. Shortening rate and Holocene surface rupture on the Riasi fault system in the Kashmir Himalaya: active thrusting within the Northwest Himalayan orogenic wedge, *Bull. Geol. Soc. Am.,* **128**(7), 1070–1094.

Gavillot, Y., Meigs, A.J., Sousa, F.J., Stockli, D., Yule, D. & Malik, M., 2018. Late Cenozoic Foreland-to-Hinterland low-temperature exhumation history of the Kashmir Himalaya, *Tectonics,* **37**(9), 3041–3068.

Ghavri, S. & Jade, S., 2021. Seismic potential of megathrust in the Kumaun-Garhwal region of NW Himalaya: implications from geodetic and seismic strain rates, *Int. J. Earth Sci.,* **110**(4), 1439–1452.

Hansman, R.J. & Ring, U., 2018. Jabal Hafit anticline (UAE and Oman) formed by décollement folding followed by trishear fault-propagation folding, *J. Struct. Geol.,* **117**, 168–185.

Harbindu, A., Gupta, S. & Sharma, M.L., 2014. Earthquake ground motion predictive equations for Garhwal Himalaya, India, *Soil Dyn. Earthq. Eng.,* **66,** 135–148.

Hardy, S. & Finch, E., 2005. Discrete-element modelling of detachment folding, *Basin Res.,* **17**(4), 507–520.

Hardy, S. & Ford, M., 1997. Numerical modeling of Trishear fault propagation folding, *Tectonics,* **16**(5), 841–854.

Hetényi, G., Cattin, R., Vergne, J. & Nábělek, J.L., 2006. The effective elastic thickness of the India Plate from receiver function imaging, gravity anomalies and thermomechanical modelling, *Geophys. J. Int.,* **167**(3), 1106–1118.

Hetényi, G., Cattin, R., Brunet, F., Bollinger, L., Vergne, J., Nábělek, J.L. & Diament, M., 2007. Density distribution of the India plate beneath the Tibetan plateau: geophysical and petrological constraints on the kinetics of lower-crustal eclogitization, *Earth planet. Sci. Lett.,* **264**(1–2), 226–244.

Heyburn, R. & Bowers, D., 2008. Earthquake depth estimation using the F trace and associated probability, *Bull. seism. Soc. Am.,* **98**(1), 18–35.

Hossler, T., Bollinger, L., Sapkota, S.N., Lavé, J., Gupta, R.M. & Kandel, T.P., 2016. Surface ruptures of large Himalayan earthquakes in Western Nepal: evidence along a reactivated strand of the Main Boundary Thrust, *Earth planet. Sci. Lett.,* **434,** 187–196.

Hough, S.E., Martin, S.S., Gahalaut, V., Joshi, A., Landes, M. & Bossu, R., 2016. A comparison of observed and predicted ground motions from the 2015 M_w 7.8 Gorkha, Nepal, earthquake, *Nat. Hazards,* **84**(3), 1661–1684.

Ingleby, T., Wright, T.J., Hooper, A., Craig, T.J. & Elliott, J.R., 2020. Constraints on the geometry and frictional properties of the Main Himalayan thrust using coseismic, postseismic, and interseismic deformation in Nepal, *J. geophys. Res.,* **125**(2), 1–26.

Jade, S. *et al.*, 2020. Crustal deformation rates in Kashmir valley and adjoining regions from continuous GPS measurements from 2008 to 2019, *Sci. Rep.,* **10**(1), 1–11.

Jouanne, F., Munawar, N., Mugnier, J.L., Ahmed, A., Awan, A.A., Bascou, P. & Vassallo, R., 2020. Seismic coupling quantified on inferred décollements beneath the Western syntaxis of the Himalaya, *Tectonics,* **39**(9), 1–20.

Joyner, W.B., 2000. Strong motion from surface waves in deep sedimentary basins, *Bull. seism. Soc. Am.,* **90**(6B), S95–S112.

Kamb, B., 1959. Petrofabric observations from Blue Glacier, Washington, in relation to theory and experiment, *J. geophys. Res.,* **64**(11), 1891–1909.

Kaneda, H. *et al.*, 2008. Surface rupture of the 2005 Kashmir, Pakistan, earthquake and its active tectonic implications, *Bull. seism. Soc. Am.,* **98**(2), 521–557.

Kennett, B.L., Engdahl, E.R. & Buland, R., 1995. Constraints on seismic velocities in the Earth from traveltimes, *Geophys. J. Int.,* **122**(1), 108–124.

Kreemer, C., Blewitt, G. & Klein, E.C., 2014. A geodetic plate motion and Global Strain Rate Model, *Geochem. Geophys. Geosyst.,* **15**(10), 3849–3889.

Kumar, S., Wesnousky, S.G., Rockwell, T.K., Briggs, R.W., Thakur, V.C. & Jayangondaperumal, R., 2006. Paleoseismic evidence of great surface rupture earthquakes along the Indian Himalaya, *J. geophys. Res.,* **111**(3), 1–19.

Kumar, S., Wesnousky, S.G., Jayangondaperumal, R., Nakata, T., Kumahara, Y. & Singh, V., 2010. Paleoseismological evidence of surface faulting along the northeastern Himalayan front, India: timing, size, and spatial extent of great earthquakes, *J. geophys. Res.,* **115**(12), 1–20.

Kundu, B., Yadav, R.K., Bali, B.S., Chowdhury, S. & Gahalaut, V.K., 2014. Oblique convergence and slip partitioning in the NW Himalaya: implications from GPS measurements, *Tectonics,* **33**(10), 2013–2024.

Lavé, J. & Avouac, J.P., 2000. Active folding of fluvial terraces across the Siwaliks Hills, Himalayas of central Nepal, *J. geophys. Res.,* **105**(B3), 5735–5770.

Lavé, J., Yule, D., Sapkota, S., Basant, K., Madden, C., Attal, M. & Pandey, R., 2005. Evidence for a great medieval earthquake (1100 A.D.) in the central Himalayas, Nepal, *Science,* **307**(5713), 1302–1305.

Lay, T., Ye, L., Koper, K.D. & Kanamori, H., 2017. Assessment of teleseismically-determined source parameters for the April 25, 2015 M_w 7.9 Gorkha, Nepal earthquake and the May 12, 2015 M_w 7.2 aftershock, *Tectonophysics,* **714-715,** 4–20.

Lu, M., Li, X.J., An, X.W. & Zhao, J.X., 2010. A preliminary study on the near-source strong-motion characteristics of the great 2008 Wenchuan earthquake in China, *Bull. seism. Soc. Am.,* **100**(5B), 2491–2507.

Maggi, A., Jackson, J.A., Priestley, K. & Baker, C., 2000. A re-assessment of focal depth distributions in southern Iran, the Tien Shan and northern India: do earthquakes really occur in the continental mantle?, *Geophys. J. Int.,* **143**(3), 629–661.

Mahesh, P., Rai, S.S., Sivaram, K., Paul, A., Gupta, S., Sarma, R. & Gaur, V.K., 2013. One-dimensional reference velocity model and precise locations of earthquake hypocenters in the Kumaon-Garhwal Himalaya, *Bull. seism. Soc. Am.,* **103**(1), 328–339.

McCaffrey, R. & Abers, G., 1988. SYN3: a program for inversion of teleseismic body waveform on microcomputers, Air Force Geophysics Laboratory Technical Report, AFGL-TR-88-0099.

McCallen, D. *et al.*, 2021. EQSIM—a multidisciplinary framework for fault-to-structure earthquake simulations on exascale computers part I: computational models and workflow, *Earthq. Spectra,* **37**(2), 707–735.

Mehta, M., Dobhal, D.P., Pratap, B., Majeed, Z., Gupta, A.K. & Srivastava, P., 2014. Late quaternary glacial advances in the Tons River Valley, Garhwal Himalaya, India and regional synchronicity, *Holocene,* **24**(10), 1336–1350.

Melton, B.S. & Bailey, L.F., 1957. Multiple signal correlators, *Geophysics,* **22**(3), 565–588.

Meza-Fajardo, K.C., Semblat, J.-F., Chaillat, S. & Lenti, L., 2016. Seismic wave amplification in 3D Alluvial Basins: 3D/1D amplification ratios from fast multipole BEM simulations, *Bull. seism. Soc. Am.,* **106**(3), 1267–1281.

Mitra, S., 2003. A unified kinematic model for the evolution of detachment folds, *J. Struct. Geol.,* **25**(10), 1659–1673.

Mitra, S., Priestley, K., Gaur, V.K. & Rai, S.S., 2006. Shear-wave structure of the South Indian lithosphere from Rayleigh wave phase-velocity measurements, *Bull. seism. Soc. Am.,* **96**(4A), 1551–1559.

Mitra, S., Kainkaryam, S.M., Padhi, A., Rai, S.S. & Bhattacharya, S.N., 2011. The Himalayan foreland basin crust and upper mantle, *Phys. Earth planet. Inter.,* **184**(1–2), 34–40.

Mitra, S., Wanchoo, S. & Priestley, K.F., 2014. Source parameters of the 1 May 2013 m$_b$ 5.7 Kishtwar earthquake: implications for seismic hazards, *Bull. seism. Soc. Am.,* **104**(2), 1013–1019.

Moisidi, M., Vallianatos, F. & Gallipoli, M.R., 2018. Assessing the main frequencies of modern and historical buildings using ambient noise recordings: case studies in the historical cities of Crete (Greece), *Heritage,* **1**(1), 171–188.

Molnar, P. & Lyon-Caen, H., 1989. Fault plane solutions of earthquakes and active tectonics of the Tibetan Plateau and its margins, *Geophys. J. Int.,* **99**(1), 123–153.

Molnar, P. *et al.*, 1994. Quaternary climate change and the formation of river terraces across growing anticlines on the north flank of the Tien Shan, China, *J. Geol.,* **102**(5), 583–602.

Mugnier, J.L., Leturmy, P., Mascle, G., Huyghe, P., Chalaron, E., Vidal, G., Husson, L. & Delcaillau, B., 1999. The Siwaliks of western Nepal I. Geometry and kinematics, *J. Asian Earth Sci.,* **17**(5–6), 629–642.

Mugnier, J.L., Vignon, V., Jayangondaperumal, R., Vassallo, R., Malik, M.A., Replumaz, A., Srivastava, R.P., Jouanne, F., Buoncristiani, J.F., Jomard, H. & Carcaillet, J., 2017. A complex thrust sequence in western Himalaya: the active Medlicott Wadia Thrust, *Quater. Int.,* **462**, 109–123.

Ni, J.F., Ibenbrahim, A. & Roecker, S.W., 1991. Three-dimensional velocity structure and hypocenters of earthquakes beneath the Hazara Arc, Pakistan: geometry of the underthrusting Indian Plate, *J. geophys. Res.,* **96**(B12), 19 865–19 877.

O'Kane, A. & Copley, A., 2021. The controls on earthquake ground motion in foreland-basin settings: the effects of basin and source geometry, *Geophys. J. Int.,* **225**(1), 512–529.

Owen, L.A., Finkel, R.C. & Caffee, M.W., 2002. A note on the extent of glaciation throughout the Himalaya during the global Last Glacial Maximum, *Quater. Sci. Rev.,* **21**(1–3), 147–157.

Pandey, A., Jayangondaperumal, R., Hetényi, G., Priyanka, R.S., Singh, I., Srivastava, P. & Srivastava, H.B., 2021. Establishing primary surface rupture evidence and magnitude of the 1697 CE Sadiya earthquake at the Eastern Himalayan Frontal thrust, India, *Sci. Rep.,* **11**(1), 1–14.

Pandey, M. & Molnar, P., 1988. The distribution of intensity of the Bihar-Nepal earthquake of 15 January 1934 and bounds on the extent of the rupture zone, *J. Nepal Geol. Soc.,* **5**(1), 22–44.

Pandey, M.R., Tandukar, R.P., Avouac, J.P., Vergne, J. & Héritier, T., 1999. Seismotectonics of the Nepal Himalaya from a local seismic network, *J. Asian Earth Sci.,* **17**(5-6), 703–712.

Parajuli, R.R. & Kiyono, J., 2015. Ground motion characteristics of the 2015 Gorkha earthquake, survey of damage to stone masonry structures and structural field tests, *Front. Built Environ.,* **1**(November), 1–12.

Paul, H., Priestley, K., Powali, D., Sharma, S., Mitra, S. & Wanchoo, S., 2018. Signatures of the existence of frontal and lateral ramp structures near the Kishtwar Window of the Jammu and Kashmir Himalaya: evidence from microseismicity and source mechanisms, *Geochem. Geophys. Geosyst.,* **19**(9), 3097–3114.

Petersson, N.A. & Sjögreen, B., 2012. Stable and efficient modeling of anelastic attenuation in seismic wave propagation, *Commun. Comput. Phys.,* **12**(1), 193–225.

Petersson, N.A. & Sjögreen, B., 2014. Super-grid modeling of the elastic wave equation in semi-bounded domains, *Commun. Comput. Phys.,* **16**(4), 913–955.

Petersson, N.A. & Sjögreen, B., 2015. Wave propagation in anisotropic elastic materials and curvilinear coordinates using a summation-by-parts finite difference method, *J. Comput. Phys.,* **299**, 820–841.

Petersson, N.A. & Sjögreen, B., 2017. SW4 v2.0 [software], Computational Infrastructure for Geodynamics, Davis, CA, doi:10.5281/zenodo.1045297.

Phillips, W.M., Sloan, V.F., Shroder, J., Sharma, P., Clarke, M.L. & Rendell, H.M., 2000. Asynchronous glaciation at Nanga Parbat, northwestern Himalaya Mountains, Pakistan, *Geology,* **28**(5), 431–434.

Pitarka, A., Gok, R., Yetirmishli, G., Ismayilova, S. & Mellors, R., 2016. Ground motion modeling in the Eastern Caucasus, *Pure appl. Geophys.,* **173**(8), 2791–2801.

Powali, D., Sharma, S., Mandal, R. & Mitra, S., 2020. A reappraisal of the 2005 Kashmir (M$_w$ 7.6) earthquake and its aftershocks: seismotectonics of NW Himalaya, *Tectonophysics,* **789**, 1–11.

Powers, P.M., Lillie, R.J. & Yeats, R.S., 1998. Structure and shortening of the Kangra and Dehra Dun reentrants, sub-Himalaya, India, *Bull. Geol. Soc. Am.,* **110**(8), 1010–1027.

Priestley, K., Jackson, J. & McKenzie, D., 2008. Lithospheric structure and deep earthquakes beneath India, the Himalaya and southern Tibet, *Geophys. J. Int.,* **172**(1), 345–362.

Priyanka, R.S. *et al.*, 2017. Primary surface rupture of the 1950 Tibet-Assam great earthquake along the eastern Himalayan front, India, *Sci. Rep.,* **7**(1), 1–12.

Rai, S.S., Priestley, K., Suryaprakasam, K., Srinagesh, D., Gaur, V.K. & Du, Z., 2003. Crustal shear velocity structure of the south Indian shield, *J. geophys. Res.,* **108**(B2), 1–12.

Rajaure, S. *et al.*, 2017. Characterizing the Kathmandu Valley sediment response through strong motion recordings of the 2015 Gorkha earthquake sequence, *Tectonophysics,* **714–715**, 146–157.

Rial, J.A., Saltzman, N.G. & Ling, H., 1992. Earthquake-induced resonance in sedimentary basins whether trapped waves are orderly or chaotic, *Am. Scient.,* **80**(6), 566–578.

Richards, B.W., Benn, D.I., Owen, L.A., Rhodes, E.J. & Spencer, J.Q., 2000. Timing of late quaternary glaciations South of Mount Everest in the Khumbu Himal, Nepal, *Bull. Geol. Soc. Am.,* **112**(10), 1621–1632.

Rodgers, A.J., Pitarka, A., Petersson, N.A., Sjögreen, B. & McCallen, D.B., 2018. Broadband (0–4 Hz) ground motions for a magnitude 7.0 Hayward Fault earthquake with three-dimensional structure and topography, *Geophys. Res. Lett.,* **45**(2), 739–747.

Rodgers, A.J., Pitarka, A., Anders Petersson, N., Sjogreen, B., McCallen, D.B. & Abrahamson, N., 2019a. Broadband (0-5 Hz) fully deterministic 3D ground-motion simulations of a magnitude 7.0 Hayward fault earthquake: comparison with empirical ground-motion models and 3D path and site effects from source normalized intensities, *Seismol. Res. Lett.,* **90**(3), 1268–1284.

Rodgers, A.J., Pitarka, A. & McCallen, D.B., 2019b. The effect of fault geometry and minimum shear wavespeed on 3D ground-motion simulations for an M$_w$ 6.5 Hayward Fault Scenario Earthquake, San Francisco Bay Area, Northern California, *Bull. seism. Soc. Am.,* **109**(4), 1265–1281.

Sapkota, S.N., Bollinger, L., Klinger, Y., Tapponnier, P., Gaudemer, Y. & Tiwari, D., 2013. Primary surface ruptures of the great Himalayan earthquakes in 1934 and 1255, *Nat. Geosci.,* **6**(1), 71–76.

Schelling, D., 1992. A balanced cross-section through the eastern Nepal Siwalik hills, Bagmati river region, implications for the structure of the southern Himalaya, *J. Nepal Geol. Soc.,* **8,** 1–10.

Schenk, V., Mantlík, F., Zhizhin, M.N. & Tumarkin, A.G., 1990. Relation between macroseismic intensity and instrumental parameters of strong motions—a statistical approach, *Nat. Hazards,* **3**(2), 111–124.

Schiffman, C., Bali, B.S., Szeliga, W. & Bilham, R., 2013. Seismic slip deficit in the Kashmir Himalaya from GPS observations, *Geophys. Res. Lett.,* **40**(21), 5642–5645.

Scholz, C.H., 1982. Scaling laws for large earthquakes: consequences for physical models, *Bull. seism. Soc. Am.,* **72**(1), 1–14.

Sharma, J., Chopra, S. & Roy, K.S., 2014. Estimation of source parameters, quality factor (Q$_s$), and site characteristics using accelerograms: Uttarakhand Himalaya Region, *Bull. seism. Soc. Am.,* **104**(1), 360–380.

Sharma, M.L., Douglas, J., Bungum, H. & Kotadia, J., 2009. Ground-motion prediction equations based on data from the Himalayan and Zagros regions, *J. Earthq. Eng.,* **13**(8), 1191–1210.

Shearer, P.M., Prieto, G.A. & Hauksson, E., 2006. Comprehensive analysis of earthquake source spectra in southern California, *J. geophys. Res.,* **111**(6), 1–21.

Singh, R.P., Aman, A. & Prasad, Y.J., 1996. Attenuation relations for strong seismic ground motion in the Himalayan region, *Pure appl. Geophys.,* **147**(1), 161–180.

Singh, S.K., Dattatrayam, R.S., Shapiro, N.M., Mandal, P., Pacheco, J.F. & Midha, R.K., 1999. Crustal and Upper mantle structure of Peninsular India and source parameters of the 21 May 1997, Jabalpur Earthquake (Mw = 5.8): results from a new regional broadband network, *Bull. seism. Soc. Am.,* **89**(6), 1631–1641.

Sjögreen, B. & Petersson, N.A., 2012. A fourth order accurate finite difference scheme for the elastic wave equation in second order formulation, *J. Sci. Comput.,* **52**(1), 17–48.

Sloan, R.A., Jackson, J.A., McKenzie, D. & Priestley, K., 2011. Earthquake depth distributions in central Asia, and their relations with lithosphere thickness, shortening and extension, *Geophys. J. Int.,* **185,** 1–29.

Srinagesh, D., Singh, S.K., Chadha, R.K., Paul, A., Suresh, G., Ordaz, M. & Dattatrayam, R.S., 2011. Amplification of seismic waves in the central Indo-Gangetic basin, India, *Bull. seism. Soc. Am.,* **101**(5), 2231–2242.

Stevens, V.L. & Avouac, J.P., 2015. Interseismic coupling on the main Himalayan thrust, *Geophys. Res. Lett.,* **42**(14), 5828–5837.

Styron, R., Taylor, M. & Okoronkwo, K., 2010. Database of active structures from the Indo-Asian Collision, *Eos,* **91**(20), 181–182.

Suppe, J., 1983. Geometry and kinematics of fault-bend folding, *Am. J. Sci.,* **283,** 684–721.

Suresh, G., Jain, S. & Bhattacharya, S.N., 2008. Lithosphere of Indus block in the Northwest Indian subcontinent through genetic algorithm inversion of surface-wave dispersion, *Bull. seism. Soc. Am.,* **98**(4), 1750–1755.

Suzuki, A. & Iervolino, I., 2017. Italian vs. worldwide history of largest PGA and PGV, *Ann. Geophys.,* **60**(5), S0551–S0551.

Takai, N., Shigefuji, M., Rajaure, S., Bijukchhen, S., Ichiyanagi, M., Dhital, M.R. & Sasatani, T., 2016. Strong ground motion in the Kathmandu Valley during the 2015 Gorkha, Nepal, earthquake, *Earth, Planets Space,* **68**(1), 1–8.

Tallett-Williams, S. *et al.*, 2016. Site amplification in the Kathmandu Valley during the 2015 M7.6 Gorkha, Nepal earthquake, *Bull. Earthq. Eng.,* **14**(12), 3301–3315.

Taylor, M. & Yin, A., 2009. Active structures of the Himalayan-Tibetan orogen and their relationships to earthquake distribution, contemporary strain field, and Cenozoic volcanism, *Geosphere,* **5**(3), 199–214.

Taymaz, T., Jackson, J. & Westaway, R., 1990. Earthquake mechanisms in the Hellenic Trench near Crete, *Geophys. J. Int.,* **102**(3), 695–731.

Thakur, V.C., Jayangondaperumal, R. & Joevivek, V., 2019. Seismotectonics of central and NW Himalaya: plate boundary-wedge thrust earthquakes in thin-and thick-skinned tectonic framework, *Geol. Soc. Spec. Publ.,* **481**(1), 41–63.

Tiwari, P., Tiwari, A. & Joshi, B., 2018. Urban growth in Himalaya: understanding the process and options for sustainable development, *J. Urban Region. Stud. Contemp. India,* **4**(2), 15–27.

Tiwari, V.M., Mishra, D.C. & Pandey, A.K., 2015. The lithospheric density structure below the western Himalayan syntaxis: tectonic implications, *Geol. Soc. Spec. Publ.,* **412**(1), 55–65.

Trifunac, M.D., 1972. Stress estimates for the San Fernando, California, earthquake of February 9, 1971: main event and thirteen aftershocks, *Bull. seism. Soc. Am.,* **62**(3), 721–750.

Vassallo, R., Mugnier, J.L., Vignon, V., Malik, M.A., Jayangondaperumal, R., Srivastava, P., Jouanne, F. & Carcaillet, J., 2015. Distribution of the Late-Quaternary deformation in Northwestern Himalaya, *Earth planet. Sci. Lett.,* **411,** 241–252.

Vignon, V. *et al.*, 2017. Sedimentation close to the active Medlicott Wadia Thrust (Western Himalaya): how to estimate climatic base level changes and tectonics, *Geomorphology,* **284,** 175–190.

Wald, D.J., Quitoriano, V., Heaton, T.H. & Kanamori, H., 1999. Relationships between peak ground acceleration, peak ground velocity, and modified Mercalli Intensity in California, *Earthq. Spectra,* **15**(3), 557–564.

Wen, R., Ren, Y., Zhou, Z. & Li, X., 2014. Temporary strong-motion observation network for Wenchuan aftershocks and site classification, *Eng. Geol.,* **180,** 130–144.

Wen, Y.Y., Ma, K.F. & Oglesby, D.D., 2012. Variations in rupture speed, slip amplitude and slip direction during the 2008 M$_w$ 7.9 Wenchuan Earthquake, *Geophys. J. Int.,* **190**(1), 379–390.

Wesnousky, S.G., Kumahara, Y., Chamlagain, D., Pierce, I.K., Karki, A. & Gautam, D., 2017a. Geological observations on large earthquakes along the Himalayan frontal fault near Kathmandu, Nepal, *Earth planet. Sci. Lett.,* **457,** 366–375.

Wesnousky, S.G., Kumahara, Y., Chamlagain, D., Pierce, I.K., Reedy, T., Angster, S.J. & Giri, B., 2017b. Large paleoearthquake timing and displacement near Damak in eastern Nepal on the Himalayan Frontal Thrust, *Geophys. Res. Lett.,* **44**(16), 8219–8226.

Wesnousky, S.G., Kumahara, Y., Nakata, T., Chamlagain, D. & Neupane, P., 2018. New observations disagree with previous interpretations of surface rupture along the Himalayan frontal thrust during the Great 1934 Bihar-Nepal earthquake, *Geophys. Res. Lett.,* **45**(6), 2652–2658.

Wessel, P., Luis, J.F., Uieda, L., Scharroo, R., Wobbe, F., Smith, W. H.F. & Tian, D., 2019. The Generic Mapping Tools Version 6, *Geochem., Geophys., Geosyst.,* **20**(11), 5556–5564.

Weston, J., Engdahl, E.R., Harris, J., Di Giacomo, D. & Storchak, D.A., 2018. ISC-EHB: reconstruction of a robust earthquake data set, *Geophys. J. Int.,* **214**(1), 474–484.

Wimpenny, S. & Watson, C.S., 2020. gWFM: a global catalog of moderate-magnitude earthquakes studied using teleseismic body waves, *Seismol. Res. Lett.,* **92**(1), 212–226.

Wu, Y.-M., Teng, T.-l., Shin, T.-C. & Hsiao, N.-C., 2003. Relationship between peak ground acceleration, peak ground velocity, and intensity in Taiwan, *Bull. seism. Soc. Am.,* **93**(1), 386–396.

Yagi, Y. & Okuwaki, R., 2015. Integrated seismic source model of the 2015 Gorkha, Nepal, earthquake, *Geophys. Res. Lett.,* **42**(15), 6229–6235.

Zwick, P., McCaffrey, R. & Abers, G., 1994. MT5 Program, *IASPEI Software Libary,* **4**.

SUPPORTING INFORMATION

Supplementary data are available at *GJI* online.

S1. Body-waveform modelling results
S2. Geomorphological analysis of the Tawi and Ravi river terraces
S3. Seismic-wave-propagation modelling material model
Figure S1. Waveform modelling of the broad-band vertical-component seismograms for the 11th January 2021 earthquake using a representative focal mechanism of 325/45/120 based on neighbouring earthquakes 12 and 13 to the east (Fig. 2 in the manuscript). The observed seismograms are shown in black and the modelled synthetics in red. Black triangles on the focal mechanism represent stations with a compressional *P*-wave arrival, whilst light grey

triangles are stations with a dilatational *P*-wave arrival. Each modelled station has a three to four letter station code (positioned in the bottom-right corner of each seismogram) and a corresponding station number on the focal sphere. The earthquake hypocentral depth and dip which yielded the best visual fit to the observed waveforms are outlined in the header panel. For events with less-constrained waveform fits, we varied the earthquake dip beyond the best-fitting value to visualise a range of dips that produced an acceptable visual fit to the broad-band waveforms. The station distribution and polarity of the *P*-wave arrivals allowed us to narrow this range of acceptable dips as the stations were constrained to their respective *P* and *T* quadrants of the focal sphere. All subsequent figures of broad-band body-waveform modelling results follow this same format.

Figure S2. Waveform modelling of the broadband (a) and short-period (b) vertical-component seismograms for the 26th February 2020 earthquake using a representative focal mechanism of 327/42/122 based on earthquakes 05 and 06 to the northwest (see Fig. 2 in the manuscript). The observed seismograms are shown in black and the modelled synthetics in red. In (b) the top three recordings illustrate a raw vertical-component seismogram from the seismic array, the stack (beam) of the array seismograms, and a band-pass filtered version of the stack. The F-statistic of Heyburn & Bowers (2008) is shown below in grey, highlighting where most energy occurs in the stack after the direct *P*-wave arrival. The bottom two panels show the normalised amplitude of the F-statistic for the horizontal slowness (*p*) and over various backazimuths (baz) to confirm that the energy after the direct *P*-wave arrival was coming from the same direction as the direct *P* arrival (which is expected for the depth phases). The dashed white line shows the backazimuth of the earthquake epicentre. The earthquake hypocentral depth which yielded the best visual fit to the observed filtered beamformed stack of seismograms and the name of the seismic array used in the body-waveform modelling is outlined in the header panel. All subsequent figures of short-period body-waveform modelling results follow this same format.

Figure S3. (a) Minimum-misfit solution for the 24th September 2019 earthquake from inverting long-period *P* and *SH* waveforms for the source–time function (STF, positioned in the bottom left corner of the bottom panel), the focal mechanism and the centroid depth (see header panel for the resultant earthquake parameters). The middle and lower panels illustrate a lower hemisphere projection of the *P* and *SH* nodal planes in the centre, surrounded by the observed (solid black lines) and modelled (dashed red lines) seismograms for each station used in the inversion, with their three to four letter station code positioned to the left of each seismogram. The pressure and tension axes were projected onto the focal sphere as a black and white circle, respectively. The two black tick marks on each seismogram show the time window over which the inversions were performed. All subsequent figures of long-period body-waveform modelling results follow this same format. (b) Sensitivity analysis tests as part of the long-period body-waveform modelling conducted for the 24th September 2019 earthquake. The header panel outlines the ranges over which the earthquake parameters (centroid depth and dip) produced an acceptable visual fit to the long-period waveforms. A lower hemisphere projection of the *P* and *SH* nodal planes and the visual fit to six seismograms (3 *P* and 3 *SH*) are shown for each test, with the source–time function (STF) and station codes positioned to the right and top of the corresponding waveforms, respectively. The observed waveforms are shown as black solid lines and the modelled synthetics are shown as red dashed lines. All subsequent figures of long-period body-waveform modelling sensitivity

analysis tests follow this same format. (c) Waveform modelling of the broad-band vertical-component seismograms for the 24th September 2019 earthquake showing the observed seismograms (black) and modelled synthetics (red) for the focal mechanism determined from the long-period body-waveform modelling (275/01/086).

Figure S4. Waveform modelling of the broadband (a) and short-period (b) vertical-component seismograms for the 13th June 2014 earthquake using a representative focal mechanism of 325/30/120 based on earthquakes 12 and 13 to the east and earthquake 01 to the north (see Fig. 2 in the manuscript). The observed seismograms are shown in black and the modelled synthetics in red. The synthetic seismograms match the observed at station IBBN with a hypocentral depth of 15 km, although a slightly shallower depth of 11.5 km matches the waveform recorded at station MORC. This difference may reflect the differential topography near the bounce points of depth phases travelling to stations IBBN and MORC. In (b) we fitted the synthetics for two hypocentral depths (11.5 and 15.5 km) and found that the synthetics for the 11.5 km depth had a better visual fit to the band-pass filtered stack of seismograms.

Figure S5. Waveform modelling of the broadband (a) and short-period (b) vertical-component seismograms for the 2nd August 2013 earthquake (at 21:37 GMT) using a representative focal mechanism of 326/42/110 after Paul *et al.* (2018). The observed seismograms are shown in black and the modelled synthetics in red.

Figure S6. Waveform modelling of the broadband (a) and short-period (b) vertical-component seismograms for the 2nd August 2013 earthquake (at 02:32 GMT) using a representative focal mechanism of 326/42/110 based on neighbouring earthquake 05 to the north (see Fig. 2 in the manuscript). The observed seismograms are shown in black and the modelled synthetics in red.

Figure S7. Minimum-misfit solution (a) and sensitivity analysis tests (b) for the 1st May 2013 earthquake from inverting long-period *P* and *SH* waveforms for the focal mechanism, centroid depth and source–time function (STF). In (a) the header panel outlines the resultant earthquake parameters and the STF is positioned in the bottom left-hand corner of the bottom panel. In (b) the header panel outlines the ranges over which the earthquake parameters (centroid depth and dip) produced an acceptable visual fit to the long-period waveforms. Waveform modelling of the broadband (c) and short-period (d) vertical-component seismograms for the 1st May 2013 earthquake showing the observed seismograms (black) and modelled synthetics (red) for the focal mechanism determined from the long-period body-waveform modelling (299/14/080).

Figure S8. Waveform modelling of the broad-band vertical-component seismograms for the 23rd August 2011 earthquake using a representative focal mechanism of 325/40/120 based on earthquakes 05 and 06 to the northwest (see Fig. 2 in the manuscript). The observed seismograms are shown in black and the modelled synthetics in red.

Figure S9. Waveform modelling of the broad-band vertical-component seismograms for the 26th May 2006 earthquake using a representative focal mechanism of 325/40/120 based on earthquakes 05 and 06 to the northwest (see Fig. 2 in the manuscript). The observed seismograms are shown in black and the modelled synthetics in red.

Figure S10. Waveform modelling of the broadband (a) and short-period (b) vertical-component seismograms for the 15th October 2005 earthquake (at 04:32 GMT) using a representative focal mechanism of 298/10/082 based on earthquake 15 along-strike to the southeast (see Fig. 2 in the manuscript). In (a) we could not deduce a hypocentral depth as there were no identifiable depth

phases in the station waveforms, albeit many clear *P*-wave arrivals. Therefore, we used the azimuthal distribution and polarity of the *P*-wave first motions picks at each station to help constrain the NE-dipping nodal plane [assuming the rake of the mechanism is 90° (i.e. a pure thrust)]. In (b) the observed seismograms are shown in black and the modelled synthetics in red.

Figure S11. Waveform modelling of the broad-band vertical-component seismograms for the 15th October 2005 earthquake (at 04:24 GMT) using a representative focal mechanism of 298/10/082 based on earthquake 15 along-strike to the southeast (see Fig. 2 in the manuscript). The observed seismograms are shown in black and the modelled synthetics in red.

Figure S12. Waveform modelling of the broad-band vertical-component seismograms for the 15th September 1993 earthquake using a representative focal mechanism of 325/42/120 based on neighbouring earthquakes 05 and 06 to the east (see Fig. 2 in the manuscript). The observed seismograms are shown in black and the modelled synthetics in red.

Figure S13. Waveform modelling of the broad-band vertical-component seismograms for the 15th September 1993 earthquake using a representative focal mechanism of 325/42/120 based on earthquakes 05 and 06 to the east (see Fig. 2 in the manuscript). The observed seismograms are shown in black and the modelled synthetics in red.

Figure S14. Waveform modelling of the broad-band vertical-component seismograms for the 26th April 1986 earthquake using a starting gCMT focal mechanism of 299/19/058. The observed seismograms are shown in black and the modelled synthetics in red.

Figure S15. Waveform modelling of the broad-band vertical-component seismograms for the 15th September 1993 earthquake. We modelled both the gCMT focal mechanism (293/10/063) and Molnar & Lyon-Caen (1989) solution (310/10/080) as our first-motion constraints until we found the best visual fit to the broad-band seismograms. The observed seismograms are shown in black and the modelled synthetics in red.

Figure S16. Waveform modelling of the broad-band vertical-component seismograms for the 1st May 1980 earthquake using a representative focal mechanism of 325/42/115 based on earthquakes 05 and 06 to the north and earthquake 07 to the northwest (see Fig. 2 in the manuscript). The observed seismograms are shown in black and the modelled synthetics in red.

Figure S17. Waveform modelling of the broad-band vertical-component seismograms for the 14th June 1978 earthquake using a representative focal mechanism of 299/20/058 based on neighbouring earthquake 14 to the northwest (see Fig. 2 in the manuscript).

The observed seismograms are shown in black and the modelled synthetics in red.

Figure S18. Waveform modelling of the broad-band vertical-component seismograms for the 7th May 1978 earthquake using a representative focal mechanism of 295/10/082 based on earthquake 03 to the south, earthquake 14 along-strike to the southeast and earthquake 15 to the east (see Fig. 2 in the manuscript). The observed seismograms are shown in black and the modelled synthetics in red.

Figure S19. Geomorphological observations in the western region of the Surin Mastgarh Anticline. (a) DEM of the topography bordering the River Tawi which flows from the Lesser Himalayan mountains through the city of Jammu, draining into the Indus basin. The blue line represents the river's course and the coloured lines represent terraces. (b) Cross-section taken parallel with the shortening direction across the region, showing the river and terrace elevations with distance along the profile A–A'. c) The terrace heights above the river with distance along the profile A–A'.

Figure S20. Geomorphological observations in the eastern region of the Surin Mastgarh Anticline. (a) DEM of the topography bordering the Ravi river's course through the Siwalik foothills, located approximately 20 km northwest of the city of Pathankot. The blue line represents the river's course and the coloured lines represent terraces. (b) The river and terrace elevations with distance along the profile A–A", taken parallel with the river's course. (c) The terrace heights above the river with distance along the profile A–A", taken parallel with the river's course. (d) The terrace heights above the river with distance along profile A'–A", taken parallel with the shortening direction across the region.

Figure S21. Averaged depth-variable profiles for the crustal properties (V_p, V_s, Q_p, Q_s and ρ), for each of the three discrete regions which make up our material model.

Figure S22. Material model used for the seismic-wave-propagation modelling in this study. The material properties are homogeneous along-strike and heterogeneous across-strike, based on a compilation of published depth-variable profiles for three distinct regions which make up our model: (1) the Indus Basin and Siwalik sediments, (2) the Indian Crust and (3) the Lesser and Higher Himalaya. (a), (b), (c), (d) and (e) illustrate the 2-D grid across-strike for material properties V_p, V_s, Q_p, Q_s, and ρ, respectively.